

Geological Society of America Bulletin

Three-dimensional (3-D) finite strain at the central Andean orocline and implications for grain-scale shortening in orogens

Nathan Eichelberger and Nadine McQuarrie

Geological Society of America Bulletin published online 30 July 2014;
doi: 10.1130/B30968.1

Email alerting services

click www.gsapubs.org/cgi/alerts to receive free e-mail alerts when new articles cite this article

Subscribe

click www.gsapubs.org/subscriptions/ to subscribe to Geological Society of America Bulletin

Permission request

click <http://www.geosociety.org/pubs/copyrt.htm#gsa> to contact GSA

Copyright not claimed on content prepared wholly by U.S. government employees within scope of their employment. Individual scientists are hereby granted permission, without fees or further requests to GSA, to use a single figure, a single table, and/or a brief paragraph of text in subsequent works and to make unlimited copies of items in GSA's journals for noncommercial use in classrooms to further education and science. This file may not be posted to any Web site, but authors may post the abstracts only of their articles on their own or their organization's Web site providing the posting includes a reference to the article's full citation. GSA provides this and other forums for the presentation of diverse opinions and positions by scientists worldwide, regardless of their race, citizenship, gender, religion, or political viewpoint. Opinions presented in this publication do not reflect official positions of the Society.

Notes

Advance online articles have been peer reviewed and accepted for publication but have not yet appeared in the paper journal (edited, typeset versions may be posted when available prior to final publication). Advance online articles are citable and establish publication priority; they are indexed by GeoRef from initial publication. Citations to Advance online articles must include the digital object identifier (DOIs) and date of initial publication.

Three-dimensional (3-D) finite strain at the central Andean orocline and implications for grain-scale shortening in orogens

Nathan Eichelberger^{1,†} and Nadine McQuarrie²

¹Department of Geosciences, Princeton University, Princeton, New Jersey 08544, USA

²Department of Geology and Planetary Science, University of Pittsburgh, Pittsburgh, Pennsylvania 15260, USA

ABSTRACT

Three-dimensional (3-D) finite strain analyses from across the central Andes are used to document the contribution of grain-scale strain in quartzites and sandstones to the total shortening budget. The results are compared to thermal, stratigraphic, and strain data from other fold-and-thrust belts to determine the influence of lithologic strength and deformation temperature on strain accommodation during orogenic evolution. In the central Andes, 3-D best-fit ellipsoids are inconsistently oriented relative to structural trends, have short axes at high angles to bedding (Z , mean plunge = $78^\circ \pm 21^\circ$), and have bedding-parallel long axes (X , mean plunge = $6^\circ \pm 24^\circ$). Ellipsoid shapes are dominantly oblate ($X = Y > Z$), indicate low natural octahedral shear strains ($\epsilon_s = 0.03\text{--}0.19$), and have axial ratios that range from 1.02:1:0.81 ($\epsilon_s = 0.19$) to 1.02:1:0.97 ($\epsilon_s = 0.03$). Highly variable R_f - ϕ data ($R_f = 1.0\text{--}5.0$, ϕ fluctuations exceeding 100°) indicate detrital grain shapes may overwhelm any measurable tectonic strain fabric recorded by grain geometry. The best-fit ellipsoids may reflect either weak compaction strain, or they may be related to a depositional fabric. At a minimum, granular strain was insufficient to reset the detrital grain fabric, and therefore grain-scale strain in quartzites and sandstones is not a significant factor in deformation. We suggest that the nonstrained nature of these stiffer lithologies indicates a lack of regional, penetrative strain in the central Andes like that quantified in similar lithologies in other orogens. The regional lack of strain may be due to deformation temperatures $<180^\circ\text{C}$ and the presence of five ≥ 1 -km-thick shale detachments. In the Sevier and Appalachian orogens, granular strain fabrics are best developed where temperatures exceeded

$\sim 180^\circ\text{C}$, but they are also found where temperatures were $<180^\circ\text{C}$. The lack of distributed detachments in Appalachian and Sevier stratigraphy may have favored minor layer-parallel shortening at temperatures $<180^\circ\text{C}$ rather than formation of numerous, low-offset faults as in the central Andes. Minimal slip on individual central Andean thrusts would have limited footwall burial and maintained low deformation temperatures.

INTRODUCTION

Quantification of strain at the granular scale in fold-and-thrust belts is a critical variable in accurately defining the kinematics of orogenic deformation. Referred to here as internal strain, grain-scale shortening can represent a significant component of the overall magnitude of shortening accommodated in an orogen (Mitra, 1994; Yonkee and Weil, 2010; Sak et al., 2012), alter the kinematic path proposed in balanced cross sections (e.g., Mitra, 1994; Sak et al., 2012), and is predicted to be a fundamental kinematic component of orocline development (Weil and Sussman, 2004; Yonkee and Weil, 2010). Globally, there are few orogen-wide finite strain data sets available, so it remains a poorly quantified aspect of fold-and-thrust belt kinematics. Where measurements have been made, granular shortening parallel to bedding (often termed layer-parallel shortening) can be as high as $\sim 20\%$ at a regional scale (e.g., Yonkee and Weil, 2010; Sak et al., 2012). Thus, internal strain can represent a substantial component of total shortening in fold-and-thrust belts but occurs at scales below the resolution of balanced cross sections (e.g., Mitra, 1994; Duebendorfer and Meyer, 2002; Yonkee, 2005; Yonkee and Weil, 2010; Sak et al., 2012). While internal strain is a critical kinematic consideration, it is essentially unique to a given fold-and-thrust belt and cannot be generalized based on currently available data.

To determine the contribution of internal strain to the total shortening budget in the cen-

tral Andes, we focus on documenting strain recorded by competent lithologies, in this case, sandstone and quartzite. The data presented here do not define a full internal strain framework, because finite strain was not measured in weak shale-based lithologies. At the scale of a single structure, finite strain accommodated in relatively low-viscosity layers (such as shale) can easily be greater and more variable than strain measured in relatively competent layers. In classical fold models involving viscosity contrasts between layers, flexural flow in low-viscosity layers results in thickening at fold hinges (Fig. 1A). Such structures are observed in the central Andes (McQuarrie and Davis, 2002), suggesting that finite strain in shale-dominated lithologies may be locally high relative to the competent quartz grain-supported layers. In other geographical locations, grain-scale shortening of the entire stratigraphic succession is interpreted to have occurred outboard of the active deformation front, largely preceding and unrelated to localized faulting and folding (e.g., Sak et al., 2012; Yonkee and Weil, 2010). In this case, the amount of total shortening must be the same for all units regardless of the way in which bulk strain was accommodated (Fig. 1B). Finite strain may be relatively high in low-viscosity shale layers as a consequence of internal distortion (Fig. 1A), but the total shortening in both competent and incompetent lithologies must be equal to maintain strain compatibility (not the case illustrated in Fig. 1B). As a result, the combined faulting, folding, and as-yet-unconstrained grain-scale shortening of competent lithologies in Bolivia most likely represent the total shortening budget. Focusing on grain-scale shortening recorded by competent lithologies provides the most robust estimate of early, layer-parallel shortening while minimizing local structural complexities related to viscosity contrasts and folding mechanisms. However, the data presented do not fully characterize the total strain recorded in the entire lithologic section.

[†]E-mail: nate@structuresolver.com

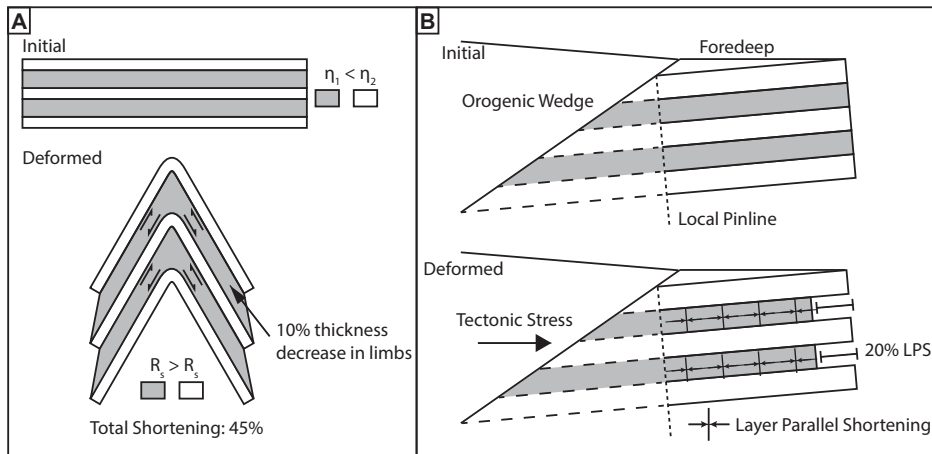


Figure 1. Structural diagrams of strain accommodation in multilayered systems with differing viscosities. (A) Mesoscale example of differing strain accommodation between low-viscosity (η_1) and high-viscosity (η_2) layers. Measured strains in the low-viscosity layer would generally be higher than those in the competent high-viscosity layer, but the total shortening for both is the same (45%). (B) Regional-scale scenario of grain-scale strain concentration within low-viscosity layers, violating strain compatibility. Layer shading indicates relative viscosity contrast as in A (η_1 , η_2). Layer-parallel shortening (LPS) at granular scale is generally interpreted to occur in front of an advancing orogenic wedge, prior to faulting and folding. If layer-parallel shortening only occurs in low-viscosity units (η_1), the lack of layer-parallel shortening in competent layers (η_2) violates strain compatibility (shown by excess competent layer length relative to incompetent layers with layer-parallel shortening). Therefore, if layer-parallel shortening is a significant component of the total shortening budget, it should be recorded in both competent and incompetent lithologies.

An understanding of the magnitude and orientation of grain-scale shortening in the central Andes is central to defining the kinematic evolution of the Bolivian orocline. Generally, orogenic curvature is best classified based on kinematic history: In primary arcs, the curvature was a preexisting feature; progressive arcs developed structural curvature concurrently with fold-and-thrust belt activity; and secondary arcs were initially linear, with structural curvature subsequently superimposed on the fold-and-thrust belt (Weil and Sussman, 2004). When the Bolivian orocline was first characterized based on the change in topographic and structural trend of the central Andes from NW-SE in southern Peru to N-S in southern Bolivia, it was considered a secondary arc. However, full differentiation between these models for any curved mountain belt requires combining bulk shortening and vertical-axis rotations with finite strain data (e.g., Weil et al., 2010; Yonkee and Weil, 2010). Where present, the pattern of mesoscale layer-parallel shortening features (such as cleavage plane orientation) and granular-scale strain markers have been used in conjunction with structural transport direction and vertical-axis rotations to distinguish between kinematic models of orocline formation (Carey, 1955; Ries and Shackleton,

1976; Marshak, 1988; Weil and Sussman, 2004; Yonkee and Weil, 2009).

In the central Andes, prior paleomagnetic (Arriagada et al., 2006; Barke et al., 2007; Roperch et al., 2006; Somoza et al., 1996) and structural studies (Kley, 1996; McQuarrie, 2002; Müller et al., 2002; Elger et al., 2005; McQuarrie et al., 2008) have constrained portions of the central Andean displacement field, but the role of internal strain has not been quantified. Paleomagnetic as well as global positioning system (GPS) data (Allmendinger et al., 2005) define a broad rotation pattern of counterclockwise rotations in the northern limb and clockwise rotations in the south limb. The fact that this is still observed in GPS data suggests that the process continues today. Overall, the orocline limbs have divergent displacement paths that predict extension at the orocline axis (Kley, 1999). There are no major extensional structures in the region; rather, the transition between the limb displacement directions appears to be accommodated by strike-slip and transpressional faults near the apex of the central Andean bend (Dewey and Lamb, 1992; Kley, 1999; Eichelberger et al., 2013). Recent reconstructions of the Bolivian orocline based on this body of data classify it as progressive arc where curvature has developed as a result of

curved deformation paths (e.g., Arriagada et al., 2008; Eichelberger et al., 2013).

The possibility remains that layer-parallel shortening at the granular scale may also accommodate significant orogeny-parallel extension. To develop an accurate kinematic history for the central Andes and create viable orocline reconstructions, layer-parallel shortening must be accounted for. If present, restoring significant layer-parallel shortening to individual thrust sheets will alter the geometry of a balanced cross section and the resulting kinematic model (i.e., Mitra, 1994). If granular strain is not accounted for, total shortening magnitudes may underestimate actual values and ultimately produce inaccuracies in the kinematics of central Andean orocline reconstructions (Kley, 1999; Hindle et al., 2005; Arriagada et al., 2008; Eichelberger et al., 2013), crustal deformation budgets (Isacks, 1988; Sheffels, 1988; Kley and Monaldi, 1998), and shortening rates (Elger et al., 2005; Barnes et al., 2008; McQuarrie et al., 2008).

In other fold-and-thrust belts where grain-scale shortening is constrained, the strain pattern is highly variable. This is presumably due to the sensitivity of strain accommodation to location-specific factors, such as mechanical stratigraphy, deformation conditions, and sample position within a given fold-and-thrust belt (Sanderson, 1982; Means, 1989; Mukul and Mitra, 1998; Yonkee, 2005; Ong et al., 2007; Long et al., 2011; Sak et al., 2012). Variability in the magnitude of grain-scale shortening can be partly attributed to the temperature and pressure dependency of intragranular and grain boundary deformation mechanisms that accommodate finite strain (e.g., Mitra and Yonkee, 1985; Hirth and Tullis, 1992, 1994; Dunlap et al., 1997; Stipp et al., 2002). Fortunately, for the orogens where strain is well documented, data sets including thermochronology, fluid inclusions, and illite crystallinity provide quantitative constraints on temperature at the stratigraphic levels where strain is measured. By expanding the global coverage of internal strain data to include the central Andean fold-and-thrust belt, we can gain new insight into granular shortening at the orogenic scale by correlating layer-parallel shortening patterns, deformation temperatures, and lithologies between different fold-and-thrust belts with similar data. Previously, individual thrust sheets have been compared based on quantitative strain parameters (e.g., Yonkee, 2005; Long et al., 2011) but never with respect to specific variables, such as temperature and mechanical stratigraphy, which may affect strain accommodation at the granular scale.

The central Andes provide a natural laboratory for evaluating the influence of deformation temperature and mechanical strength on

layer-parallel shortening in sandstone and quartzite lithologies at the grain scale. Numerous studies from the orocline axis region have indirectly constrained maximum deformation temperatures through thermochronology (Benjamin et al., 1987; Gillis et al., 2006; Barnes et al., 2006, 2008; Ege et al., 2007; McQuarrie et al., 2008). In addition, the stratigraphic section involved in Andean deformation is well documented, including regional variations and stratigraphic position of important detachments (Roeder and Chamberlain, 1995; Sempere, 1995; Welsink et al., 1995; Gonzáles et al., 1996). Determining how strain varies between stratigraphic levels, structural packages, and over different temperature conditions across fold-and-thrust belts can help us to evaluate the relative importance of these factors in accommodating grain-scale shortening. Comparisons of these variables between orogens offer an opportunity to constrain the fundamental thermal and mechanical controls on the way in which strain is accommodated and recorded during orogenic evolution.

This study presents new three-dimensional (3-D) finite strain data from across the central Andean orocline axis to assess the contribution of grain-scale shortening to the total shortening budget. We interpret apparent internal strain from best-fit 3-D ellipsoids (Mookerjee and Nickleach, 2011) based on two-dimensional (2-D) ellipses measured by the normalized Fry method (Erslev, 1988). The R_f - ϕ method is also used to determine the variability in individual grain shape and to document the potential influence of detrital grain geometry on the best-fit ellipsoids. We note that at low strains, the influence of detrital grain geometry may exceed any detectable tectonic strain, in which case, best-fit 2-D and 3-D ellipses/ellipsoids reflect the average grain shape rather than a strain ellipsoid. The 3-D ellipsoid shapes are used to quantify apparent strain magnitude (octahedral shear strain, ϵ_s) and strain state (Flinn's k -value). There are two main objectives in quantifying internal strain in the central Andes:

(1) to define the extent to which grain-scale shortening of competent lithologies in the central Andes has contributed to orocline formation and plateau evolution; and

(2) to determine potential orogen-scale factors that influence how grain-scale shortening recorded in relatively competent lithologies contributes to total shortening budgets of the Sevier, Appalachian, and central Andean fold-and-thrust belts.

To do so, we compare stratigraphic variations in deformation temperature, mechanical properties, and strain measured in competent lithologies between regions.

GEOLOGIC BACKGROUND

At the Bolivian orocline axis, there are five physiographic regions (W to E): the modern volcanic arc at the Western Cordillera; the high-elevation Altiplano basin; the Eastern Cordillera; Interandean zone; and Subandes (Fig. 2; Isacks, 1988; Kley, 1996). The strain samples presented in this study come from the retro-arc fold-and-thrust belt, where the majority of regional shortening is accommodated by thrust faults and folds within the Eastern Cordillera, Interandean zone, and Subandes (i.e., Kley, 1996; McQuarrie, 2002; Müller et al., 2002). In general, exhumation and deformation in the Eastern Cordillera initiated by ca. 40 Ma and progressed eastward over time to the modern orogenic front at the Subandes–foreland basin boundary (e.g., Barnes and Ehlers, 2009).

Regionally, both fold-and-thrust belt width and shortening estimates reach a maximum near the axis of the central Andean orocline and decrease northward into Peru and southward toward Argentina (i.e., Isacks, 1988; Kley and Monaldi, 1998; McQuarrie, 2002). The rocks involved in deformation are a continuous, ~15-km-thick section of Ordovician through Devonian marine siliciclastic rocks with an intermittently preserved section of Carboniferous through Cretaceous nonmarine siliciclastics and carbonates (Roeder and Chamberlain, 1995; Sempere, 1994, 1995; Gonzáles et al., 1996). The Paleozoic section is marked by at least three upward-coarsening sequences where weak shale grades upward into competent sandstone and quartzite. These are interpreted to be the result of major marine transgressions that deposited the stratigraphically continuous Ordovician Capinota, Silurian Uncia, and Devonian Belen shale packages (Fig. 3; Sempere, 1995). Interspersed between these units are numerous formations characterized by shale and sandstone interbedded at high frequency (e.g., Silurian Catavi, upper Devonian formations). In fact, the Ordovician San Benito and Devonian Vila Vila Formations are the only packages of uninterrupted, competent quartzite and sandstone deposited on a regional scale at the orocline axis. The shale horizons result in as many as seven detachments at various stratigraphic levels throughout the central Andes in Bolivia (McQuarrie, 2002; Müller et al., 2002). Penetrative strain features such as pencil structures, bed-parallel dissolution cleavage, and axial planar cleavage have been observed primarily in shale-rich stratigraphy located in the western Eastern Cordillera, but are limited to areas near thrust fault-tip lines (McQuarrie and Davis, 2002). Slaty cleavage, proposed to be a product of both pre-Andean and Andean short-

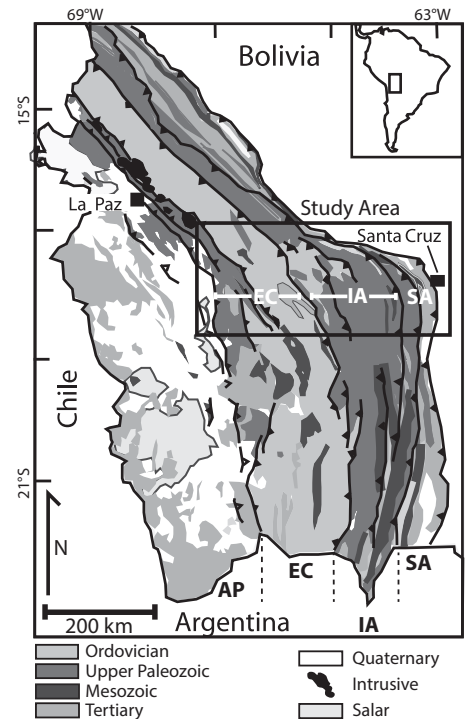


Figure 2. Simplified geologic map of the Bolivian central Andes (modified from McQuarrie, 2002). Strain samples were collected from the boxed-in study area. The approximate structural boundaries of the physiographic regions are indicated at the south end of the map area. The zones shown are: Altiplano (AP), Eastern Cordillera (EC), Interandean zone (IA), Subandes (SA).

ening, has been observed in low-grade metamorphic Ordovician strata in the Eastern Cordillera of southern Bolivia (Müller et al., 2002). While penetrative strain is localized, the majority of the shortening in the Bolivian Andes is accommodated by tight folding (wavelengths of 5–15 km) and thrust faults (average offset ≤ 10 km) spaced at structural wavelengths of 30 km or less that offset the oversteepened limbs of fault propagation folds (McQuarrie, 2002; Müller et al., 2002; McQuarrie et al., 2008; Eichelberger et al., 2013). Fold and fault spacing is generally greater in the Subandes and Eastern Cordillera, more densely spaced in the Interandean zone, and densest in the western Eastern Cordillera back-thrust region (McQuarrie and DeCelles, 2001).

FINITE STRAIN ANALYSIS

Samples for finite strain analysis were collected along and between two across-strike structural transects located between 17°S and 18.75°S. One transect extends across the axial region (Eichelberger et al., 2013), while the

		Lithology ¹	Mechanical Characterization ²	
TERTIARY	Synorogenic Sediments	Sandstone, conglomerate Some siltstone, shale, and gypsum	Stiff	
J/K		Sandstone, siltstone, shale and gypsum	C: Soft J: Stiff	
C		Sandstone, shale, limestone	Moderate	☆
DEVONIAN	Iquiri Huamapampa Los Monos Colpacucho	Alternating sandstone and shale	Moderate Soft Stiff	☆
	Icla/Belen	Shale	Soft	
	Sta. Rosa/ Vila Vila	Sandstone	Stiff	☆
	Tarabuco/ Catavi	Alternating sandstone and shale	Moderate	☆
SILURIAN	Krusillias/ Uncia	Shale	Soft	
	Llallagua		Stiff	☆
	Cancaniri	Diamictite and shale	Soft	
ORDOVICIAN	San Benito	Sandstone, quartzite	Stiff	☆
	Anzlado	Metasiltstone	Stiff → Soft	☆
	Capinota	Shale and phyllite	Soft	

☆ : 3-D strain data in this study → : Major detachment horizon
 1: From McQuarrie (2002) C: Carboniferous
 2: From McQuarrie and Davis (2002) J/K: Jurassic/Cretaceous

Figure 3. Simplified stratigraphic column from McQuarrie (2002, and references therein). Mechanical characterization is from McQuarrie and Davis (2002) based on rock properties from Jaeger and Cook (1979). Stars represent stratigraphic levels sampled for finite strain analysis for this study.

other is immediately north of the bend (Fig. 4; McQuarrie, 2002). Given the friability of the mudstone, shale, and slate lithologies interspersed throughout the stratigraphy at this latitude, sampling ultimately focused on units featuring quartz grain-supported sandstone and quartzite beds (Fig. 3). Samples from units

younger than Carboniferous were either too poorly lithified to sample or disintegrated during cutting and polishing. For each sample, three 2-D grain shape analyses were made on three orthogonal planes. A 3-D best-fit ellipsoid was then fitted to these data and used to interpret 3-D finite strain.

Sample Preparation

Oriented samples were collected from quartz grain-supported sandstone and quartzite beds. Since pervasive tectonic foliations were not present in the central Andes, cut planes for 2-D strain analysis were oriented based on bedding orientation alone. For each sample, planes were cut parallel to dip direction (A planes), strike direction (B planes), and bedding (C planes). All images were made with the in situ bedding orientation structurally restored to horizontal, accomplished by rotating the sample around the orientation of bed strike by the dip magnitude. By restoring sample orientations based on the local structure, we can determine if additional complexity in the restoration path (such as vertical-axis rotations or transpression) is required to explain differences in granular principal strain axis orientation and bulk shortening directions inferred from regional structural trends. Thus, A and B plane images and grain shape plots are stratigraphic-up, and C-plane images are viewed looking down on the bed surface. Three cross-polarized light (CPL) photomicrographs were collected at horizontal, -30° , and $+30^\circ$ for each plane (Fig. 5A) and merged into a single image to highlight grain boundaries and image quartz grains regardless of variable extinction angles (after Long et al., 2011). Additionally, scanning electron microscope-cathodoluminescence (SEM-CL) images (Fig. 5B) were collected for side-by-side strain analyses with polarized light images.

Fry and R_f - ϕ Methods

Due to the prevalence of fine- to medium-grained sandstone and quartzite and the relative scarcity of deformed fossiliferous, calcareous, or diamictite units in the central Andes, we relied on the normalized Fry method (Erslev, 1988) to measure finite strain ellipses. The Fry method measures the separation distance between grain centers in a close-packed aggregate (Fig. 5C; Fry, 1979; Ramsay and Huber, 1983). For anticlustered aggregates, the Fry plot has a central void defined by the minimum distance between grain centers. The elliptical shape of the void is related to the anisotropic distribution of grain locations due a combination of matrix strain, mass transfer processes, and initial grain shape (Fig. 5D; Fry, 1979; Ramsay and Huber, 1983). Normalizing the grain center separation distance of all grain pairs by the sum of each grain-pair radii tends to produce a dense ring around the central void that can be fit by an ellipse (Erslev, 1988). Assuming that the grains had an initially isotropic, anticlustered distribution, the best-fit ellipse reflects the magnitude and orientation of the penetrative strain field

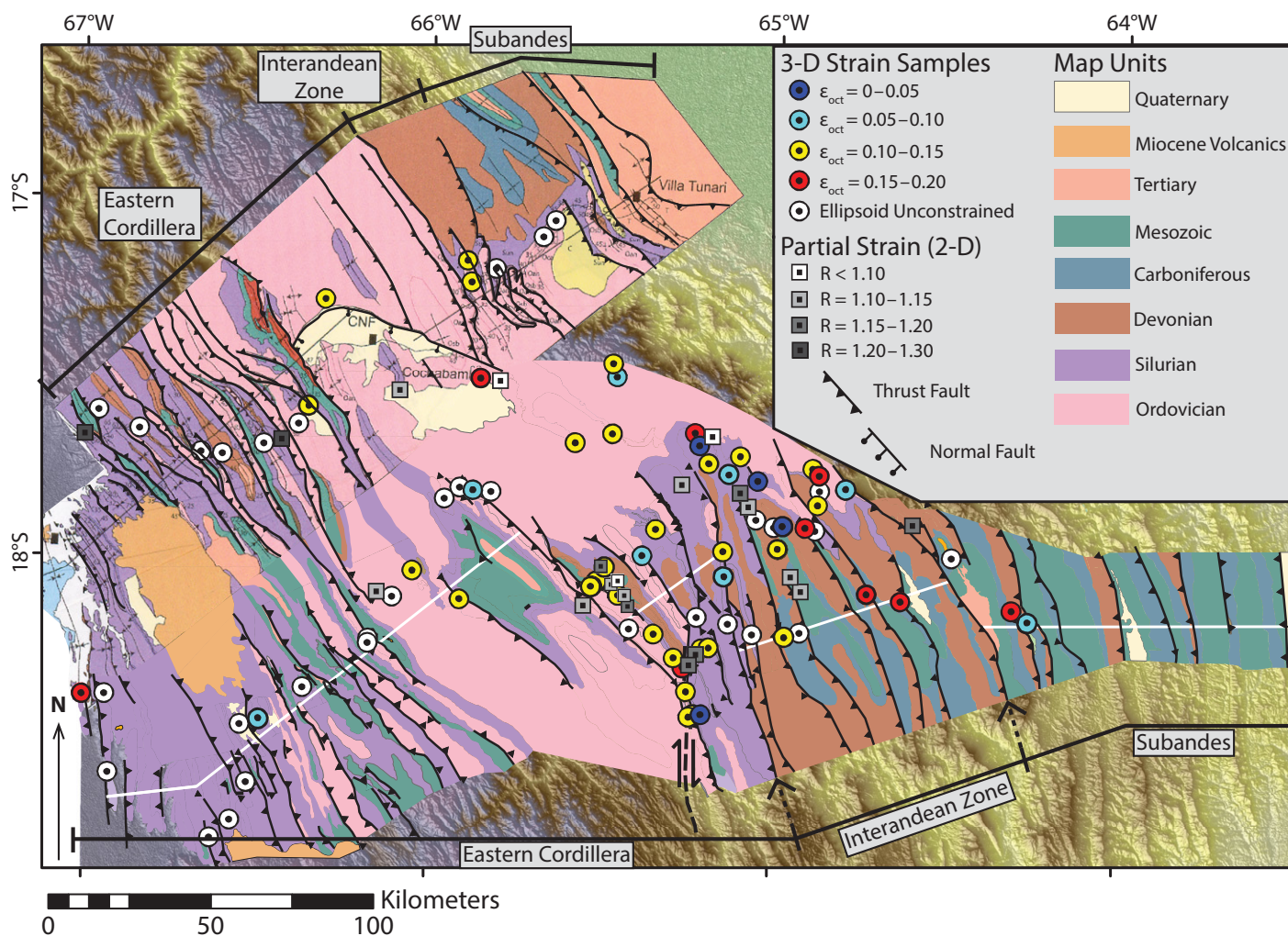


Figure 4. Advanced Spaceborne Thermal Emission and Reflection Radiometer (ASTER) 30 m digital elevation model (DEM) with geologic mapping from McQuarrie (2002) and Eichelberger et al. (2013). Locations of strain samples presented in this study are noted. White circles represent samples where full three-dimensional (3-D) finite strain ellipses could not be determined due to sample preparation problems. Colored circles are ramped according to ϵ_s magnitude, with blue reflecting low strains and red reflecting higher strains. Squares indicate the location of samples with partial strain data (A, B, and/or C planes) and are gray-scale ramped based on two-dimensional (2-D) strain. For samples with two planes, the larger of two R values is used.

experienced by the sample (Fig. 5D). The ellipticity (R_s) is the axial ratio of the long to short axial lengths and approximates the magnitude of strain, while the inclination (ϕ) is the angle between the long axis and bedding, and it is used to characterize the type of strain recorded (Ramsay and Huber, 1983). In addition, R_s - ϕ analyses were performed for a subset of samples to determine the variability in grain shape orientation in the same data used for the Fry method. The R_s - ϕ method compares the ratio of the long to short grain dimensions (R_s) and the orientation of the long dimension relative to bedding (ϕ ; e.g., Ramsay and Huber, 1983). Best-fit 2-D ellipses were determined from R_s - ϕ data using the eigenvalue method (Shimamoto and Ikeda, 1976) implemented in EllipseFit 2 (Vollmer,

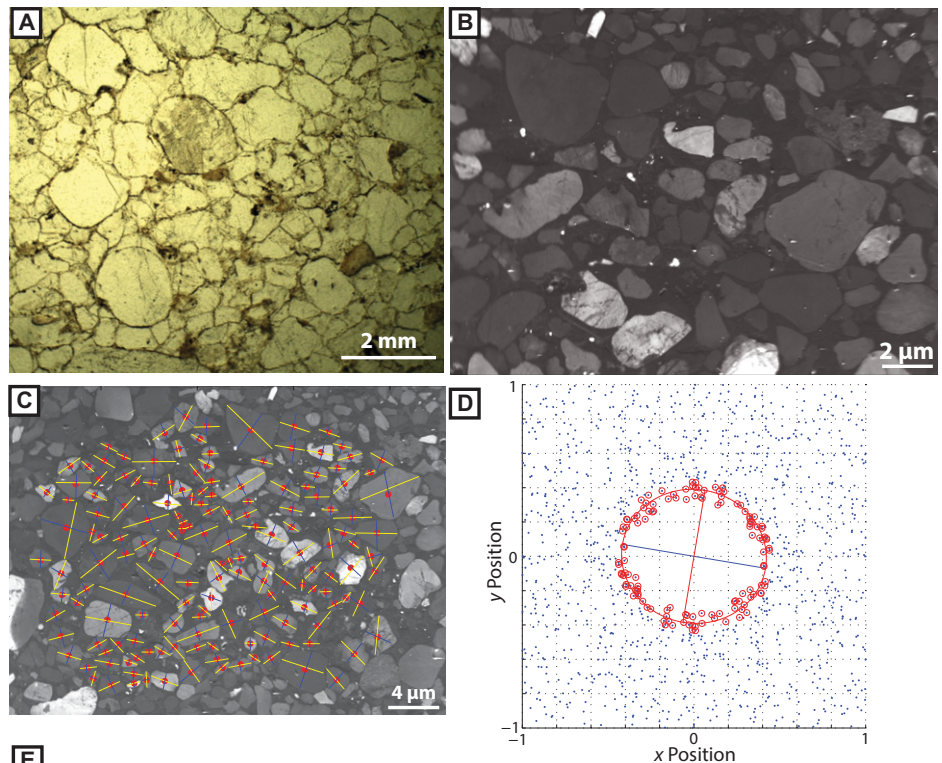
2010, 2011a, 2011b) in order to compare the results against 2-D ellipses determined by the Fry method. While the Fry measures the bulk distribution of grain centers, the R_s - ϕ method measures the range of individual grain shapes. Samples with highly variable grain orientations have a range of ϕ greater than 90° (referred to as fluctuation, F) and are heavily influenced by the initial grain shape (R_i) to the point that it exceeds any granular ellipticity related to tectonic strain (R_s ; Ramsay and Huber, 1983).

2-D Strain Measurement

From the photomicrographs of each plane, grain centers and long and short axes were manually picked for >150 close-packed grains

and used to create a normalized Fry plot in Matlab (Figs. 5C and 5D). A direct least-squares estimation of the conic ellipse equation (Fitzgibbon et al., 1999; Gal, 2003) was iteratively applied to the individual points in the Fry plot to remove exterior points until only the central high-density ring remained. The process records the best-fit ellipse parameters for each iteration and stops before the remaining points drops below $n = 100$ (Fig. 5E). Planes with greater ellipticity will converge toward specific ϕ and R_s values, whereas plots with lower eccentricities will converge to $R_s \approx 1$ but variable ϕ (Fig. 5E). Normalized residual sum of squares (RSS) was also recorded to compare ellipse fit between subsequent iterations. Of the final two iterations, the ellipse with the lowest RSS was taken as the

Figure 5. Thin-section images and Fry analyses of sample EC20, an Ordovician quartzite. All thin-section images are oriented parallel to bedding. (A) Plane polarized light image of quartzite with impinging grain boundaries and limited suturing. (B) Scanning electron microscope–cathodoluminescence (SEM-CL) image of the same thin section, but different region. Dark-gray areas between detrital cores are cement overgrowths. (C) Fry analysis of SEM-CL image, excluding cement overgrowths. Red points are user-selected grain centers, yellow lines are long axes, and blue lines are short axes. (D) Fry plot from SEM-CL image in C. Circled points indicate those used to achieve the best-fit ellipse shown, where $x = 0$ is bedding parallel. Axial units are arbitrary and used to determine ellipse aspect ratio. (E) Output of ellipse parameters in the iterative ellipse-fitting process used to eliminate the exterior points (uncircled points in C). The final two iterations have similar axial lengths and inclinations.



best fit. Uncertainties in the ellipse parameters (R_s and ϕ) for the final fit were then determined by fitting ellipses to 1000 bootstrap resamples of the central point ring.

SEM-CL Imaging

The accuracy of using the Fry method to measure apparent strain magnitude is dependent on not only meeting the initial grain center distribution assumptions discussed already, but also being able to fully image the grain boundaries in order to locate the grain centers. A potential complicating factor is that pressure solution and quartz cement overgrowths not visible in CPL can obscure the original grain shape and skew strain results, especially in fine-grained sandstones where pressure solution can be significant (Houseknecht, 1988; Dunne et al., 1990). To determine if overgrowths were present in the central Andes, a pilot suite of samples from across the study area were imaged using SEM-CL in addition to standard CPL images. The SEM-CL images were collected using a Gatan MiniCL detector and a XL30 SEM with an accelerating voltage of 25 kV at Princeton University's Imaging and Analysis Center. Cement overgrowths were present, and a few discontinuous dissolution surfaces and veins were observed, but neither occurred frequently enough to determine systematic orientations (Figs. 5A and 5B). Fry analyses of CL and CPL images of the same thin section had R_s and ϕ

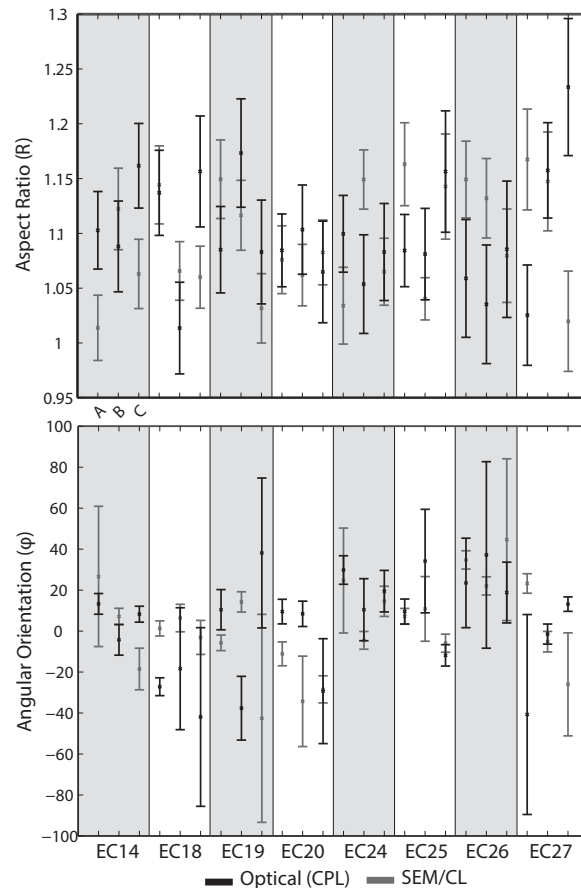
values that did not systematically vary within 1σ and were statistically equivalent within 2σ (Fig. 6). Because there was no significant difference between strain results from the two imaging techniques, the remaining strain measurements were made on CPL images.

3-D Strain Ellipsoid Fitting

From the 2-D best-fit ellipses of the A, B, and C planes for each sample, the short axis length, long axis length, inclination, planar orientation, and respective uncertainties were used to constrain a best-fit 3-D ellipsoid using Geologic Programs for Mathematica (Mookerjee and Nickleach, 2011). The program employs a least-

squares approach to minimize error between the input planar ellipses (A, B, C planes) and the corresponding sectional ellipse through the best-fit 3-D ellipsoid (Mookerjee and Nickleach, 2011). The program quantifies the difference between the input 2-D ellipsoids and the best-fit 3-D ellipsoid by reporting a scalar "mean error" that is proportional to the goodness of fit, with 0 indicating a perfect fit (Mookerjee and Nickleach, 2011). Error margins for the ellipsoid shape parameters and principal axes orientations are estimated based on the variability of 1000 simulated ellipsoids fit to randomly drawn input 2-D ellipse parameters (R_s , ϕ , and planar orientation) from a distribution based on the actual 2-D parameter uncertainties (Mookerjee

Figure 6. Comparison of best-fit two-dimensional (2-D) ellipse parameters (2σ uncertainties) for grain shape data measured from cross-polarized light (CPL) and scanning electron microscope–cathodoluminescence (SEM-CL) images. Samples are spread across the Eastern Cordillera and Eastern Cordillera back thrust. The results are plotted alphabetically for each sample: strike parallel (A-cuts), dip parallel (B-cuts), and bedding parallel (C-cuts).



and sutured grain boundaries are poorly developed, if present at all, and isolated to just a few adjacent grains (Figs. 5A and 5B). These observations are conceptually consistent with the low apparent strains measured in thin section.

Results for 22 additional samples with partial strain data (1–2 planes) are reported in Table 2 and located in Figure 4. In general, the 2-D strain results are characterized by mean strain ratios of 1.12 ± 0.05 for A planes and 1.11 ± 0.05 for B planes. The 2-D ellipse long axes are nearly horizontal with respect to bedding (θ) in both A and B planes (mean θ is $16^\circ \pm 10^\circ$ and $18^\circ \pm 13^\circ$, respectively). These 2-D results are typical for all of the samples collected and record very low strain magnitudes. In light of the low strain magnitudes measured in both the 3-D and 2-D data, the long (X) and short axes (Z) may simply reflect the dimensions of preserved detrital grain shapes rather than principal strain axis orientations.

R_f - ϕ versus Fry Results

A subset of samples was selected for R_f - ϕ analysis based on regional distribution, relatively large strains ($\epsilon_s > 0.10$), prolate ellipsoid shape, and X -axes oblique to subparallel to bedding. In thin section, all samples had large variations in grain size and orientation, which resulted in substantial data dispersion in R_f - ϕ plots. Comparison of the best-fit ellipse results between the Fry and R_f - ϕ methods shows that both measure equivalent ellipse orientations within uncertainty (Fig. 7A), whereas best-fit R_f - ϕ ellipses have nearly equivalent, but consistently higher, R_s magnitudes (Fig. 7B). Since the both methods have largely identical best-fit ϕ values, the best-fit 3-D ellipsoids have equivalent principal axis orientations within uncertainty. A detailed example (sample IA5) is shown in Figure 8, where the R_f - ϕ best-fit R exceeds the best-fit Fry R . The R_f - ϕ data from IA5 have a weak peak in point density near $\phi = 0$ but show a broad range of R_f values (1.0–>3.0) and large long axis fluctuations ($F > 100^\circ$), consistent with the wide variety of grain shapes and orientations seen in the thin sections (Fig. 8). Relative to other R_f - ϕ results, data from IA5 show a typical range of R_f values but have the lowest fluctuation (C plane, $F = 108^\circ$) of the subset. Many samples show even greater scatter in the data, characterized by R_f - ϕ plots with $F = 160^\circ$ – 180° and best-fit ϕ values that conflict with Fry best-fit ϕ (Fig. 7). Based on the criteria of Ramsay and Huber (1983), such high fluctuations indicate that initial grain ellipticities overwhelm any measurable tectonic strain ($R_f > R_s$).

The standard R_f - ϕ equations for determining R_f and R_s for situations where $F > 90^\circ$ are

and Nickleach, 2011). Ultimately, the orientation of the best-fit 3-D ellipsoid is used to infer the trend/plunge of the principal strain axes. The ellipsoid shape parameters are used to interpret the average magnitude of strain (ϵ_s octahedral shear strain; Nadai, 1963) and type of strain (Flinn's k -value; Flinn, 1962).

RESULTS

Of 106 samples collected in the field, 56 were sufficiently indurated to provide the three planes necessary to constrain the 3-D ellipsoid (Fig. 4). For unsuccessful samples, at least one plane (usually bedding parallel) disintegrated during thin-section preparation. The 3-D ellipsoid fits based on data from just two planes produced results with unacceptably high variability in principal axis orientations and ellipse shape parameters such that no specific kinematic interpretation was feasible. However, the 56 samples with well-constrained ellipsoids represent nearly the full stratigraphic column exposed at the orocline core (Table 1). The notable exception is the Subandes, where samples were impossible to collect or prepare due to the high degree of weathering and minimally lithified nature of the Carboniferous, Mesozoic, and Tertiary units exposed there.

The mean error between the input 2-D data and best-fit 3-D ellipsoids ranges from 0.01 to 0.19, indicating acceptable fits (Table 1). Uncertainties for principal axial orientations range from 1° to 90° for long and intermediate axes, while the angular error for short axes is much lower (1° – 32°). Average apparent strain magnitudes for the 3-D ellipsoids range from $\epsilon_s = 0.03$ to 0.19 with uncertainties between 0.01 and 0.05. Ellipsoid shapes span the full range from prolate ($k \geq 1.0$) to oblate ($k < 1.0$), with k -values from 0.1 to 22.3, which correspond to a range of triple-axial ratios ($X:Y:Z$) from 1.23:1:0.99 ($\epsilon_s = 0.17 \pm 0.01$, $k = 22.3 \pm 10$) to 1.02:1:0.81 ($\epsilon_s = 0.19 \pm 0.03$, $k = 0.1 \pm 0.1$). From outcrop observations, there is a notable lack of pervasive foliation as well as minimal cleavage development. Bedding involved in tight minor folds frequently featured slickenlines consistent with flexural slip (McQuarrie and Davis, 2002) but no well-developed axial planar cleavage. Minor intraformational thrust faulting was also observed but only in close proximity to major regional fold and fault zones. At the microscale, quartz grains were mantled with cement and weak undulose extinction but exhibited no visually discernible preferential alignment. Microstructural features such as dissolution surfaces

highly sensitive to the largest and smallest R_f values and are thus easily skewed by outliers, especially here where grain shapes are so variable (see micrographs in Fig. 8). Here, we report best-fit R_f - ϕ ellipses in Figures 6 and 7, which are less sensitive to such outliers. Even so, the large mean R_f (with equally large uncertainties), along with visual inspection of the micrographs and R_f - ϕ plots (Fig. 8), gives a better indication of grain shape variability than the best-fit parameters and 2σ confidence intervals alone (Fig. 7). Overall, the significant dispersion in grain shape may be responsible for overestimated R_f - ϕ strain values due to the variable grain sizes present in many thin sections. In contrast, the normalized Fry method is less sensitive to individual grain variations, especially in situations where orogenic strain is low. In the end, the R_f - ϕ results indicate that the apparent strains measured by both methods are heavily influenced by the detrital geometry.

Axial Orientations

The in situ strain ellipsoid axial orientations from across the orocline region show considerable variability in orientation (Fig. 9). Neither the X axes nor the Z axes show preferential alignment along a specific trend. Stereonet 8.9.2 (Allmendinger et al., 2013; Cardozo and Allmendinger, 2013) was used to calculate the Bingham axial distributions (Fisher et al., 1987) and Kamb contours (Kamb, 1959) for the regional data set in order to determine mean orientations and point concentration. For the Bingham axial distribution, the first eigenvector was interpreted to reflect the mean axial orientation, and the third eigenvector was used to locate orientations with the lowest point density. The in situ axes show broad variations in orientation, but generally the X axes weakly cluster around low plunges, and the Z axes weakly cluster at higher plunges (Fig. 9A). The X axes have the lowest point density around higher plunges, while the reverse is true for the Z axes (eigenvector 3 in Fig. 9A). The dispersion in axial plunge for both sets of axes is greatly reduced by restoring them to bedding-horizontal (rotation around bedding strike by dip magnitude), as indicated by greater eigenvalues for the mean axial orientations (eigenvector 1, Fig. 9B) as well as a decreased eigenvector α_{05} error ellipse. In this reference frame, ellipsoid axes with $P = 0^\circ$ are parallel to bedding and those with $P = 90^\circ$ are perpendicular to bedding. The restored X axes are generally subparallel to bedding ($P < 45^\circ$) and have a mean trend/plunge and minimum/maximum error ellipse of $098/04^\circ \pm 8^\circ/11^\circ$. The restored Z axes are dominantly bedding-oblique to -perpendicular ($P > 45^\circ$) with a

TABLE 1. THREE-DIMENSIONAL (3-D) STRAIN RESULTS

ID	Long (°W)	Lat (°S)	Strike (°)	Dip (°)	Sect. T*	Unit†	Axial length			Mean error [§]	$\epsilon_s^\#$	ϵ_s error	Flinn's k^{**}		k error	X orientation			Y orientation			Z orientation			
							X	Y	Z				+	-		T ^{††} (°)	P ^{§§} (°)	Err.##	T (°)	P (°)	Err.	T (°)	P (°)	Err.	
Subandes																									
SA1	64.31	18.12	32	21	90	C	1.23	1	0.99	0.04	0.17	0.01	0.01	22.3	9.8	7.7	185	18	1	296	47	10	80	37	10
SA2	64.26	18.15	144	60	90	C	1.08	1	0.98	0.01	0.07	0.00	0.00	4.0	1.4	0.7	128	5	1	220	21	2	24	69	2
SA3	67.14	15.40	98	42	55	Du	1.03	1	0.86	0.07	0.14	0.02	0.03	0.2	1.4	0.1	103	33	32	211	26	32	332	46	9
SA4	67.16	15.42	83	28	55	C	1.03	1	0.86	0.01	0.13	0.00	0.00	0.2	0.0	0.1	145	23	7	243	16	7	4	61	1
Interandean zone																									
IA1	64.63	18.09	112	35	72	C	1.08	1	0.84	0.07	0.18	0.01	0.00	0.4	0.0	0.0	32	10	2	125	14	2	267	73	1
IA2	64.73	18.08	147	25	72	D	1.05	1	0.84	0.03	0.17	0.00	0.00	0.3	0.0	0.0	44	31	2	307	11	2	200	57	1
IA3	64.79	17.79	317	61	72	Sc	1.07	1	0.94	0.08	0.09	0.01	0.01	1.0	0.5	0.3	121	1	4	211	7	4	24	83	3
IA4	64.87	17.75	108	17	72	Osb	1.05	1	0.85	0.03	0.16	0.00	0.02	0.3	0.0	0.3	61	2	50	152	28	51	327	62	4
IA5	64.89	17.73	298	23	72	Oa	1.09	1	0.93	0.14	0.11	0.01	0.00	1.2	0.2	0.2	358	6	4	256	63	4	91	26	3
IA6	64.88	17.83	146	19	72	Dv	1.08	1	0.93	0.05	0.11	0.00	0.02	1.0	0.0	0.8	269	12	33	178	5	33	65	77	4
IA7	64.91	17.90	117	18	72	Sc	1.10	1	0.89	0.04	0.15	0.00	0.05	0.8	2.3	0.2	90	3	82	182	42	82	357	48	20
IA8	64.98	17.89	149	30	72	Dv	1.02	1	0.97	0.18	0.03	0.04	0.00	0.6	0.7	0.2	55	38	87	156	13	90	261	49	32
IA9	64.99	17.96	162	40	72	Dv	1.13	1	0.93	0.07	0.14	0.01	0.01	1.8	0.6	0.4	113	31	2	203	1	2	295	59	2
IA10	64.97	18.20	172	35	72	C	1.13	1	0.97	0.19	0.11	0.01	0.01	4.3	3.6	1.8	300	29	2	40	16	3	155	56	3
IA11	65.05	17.77	23	58	72	Osb	1.02	1	0.97	0.13	0.03	0.01	0.01	0.5	0.2	0.2	256	2	10	164	52	11	348	38	7
IA12	65.10	17.70	183	19	72	Sc	1.08	1	0.89	0.05	0.13	0.00	0.00	0.6	0.1	0.1	163	19	1	254	3	2	354	71	1
IA13	65.23	17.64	26	28	72	Sc	1.12	1	0.90	0.10	0.15	0.01	0.01	1.1	0.3	0.2	163	15	2	59	44	2	268	42	2
IA14	65.22	17.67	292	25	72	Sc	1.02	1	0.95	0.06	0.05	0.00	0.00	0.4	0.2	0.2	80	1	6	170	7	6	341	83	2
IA15	65.19	17.72	187	75	72	Dv	1.14	1	0.98	0.11	0.12	0.01	0.00	6.0	1.4	1.1	251	9	2	353	53	10	154	35	10
IA16	65.13	17.75	30	47	72	Sc	1.05	1	0.94	0.19	0.08	0.01	0.00	0.8	0.2	0.2	308	32	5	55	26	5	177	47	4
IA17	65.18	17.82	2	15	72	Dv	1.05	1	0.86	0.04	0.14	0.00	0.00	0.3	0.0	0.0	53	10	4	144	3	4	248	79	1
IA18	65.15	17.97	149	67	72	Sc	1.06	1	0.90	0.11	0.12	0.01	0.01	0.5	0.3	0.2	175	18	6	271	17	6	41	65	2
IA19	65.14	18.04	189	41	72	Sc	1.05	1	0.95	0.06	0.07	0.00	0.00	0.9	0.1	0.1	218	16	1	318	32	2	105	54	2
IA20	65.89	17.23	163	22	55	Osb	1.08	1	0.93	0.04	0.10	0.01	0.02	1.1	0.4	0.7	264	19	43	167	20	46	33	62	15
IA21	65.90	17.17	282	38	55	Osb	1.02	1	0.85	0.04	0.14	0.00	0.01	0.1	0.4	0.0	116	39	13	228	25	12	341	41	6

(continued)

Andean orocline strain and orogen-scale factors influencing grain-scale shortening

TABLE 1. THREE-DIMENSIONAL (3-D) STRAIN RESULTS (continued)

ID	Long (°W)	Lat (°S)	Strike (°)	Dip (°)	Sect. T*	Axial length			Mean error [§]	ε _s error		Flinn's k**		k error		X orientation			Y orientation			Z orientation		
						X	Y	Z		Unit†	ε _s	+	-	k	+	-	T†† (°)	P ^{§§} (°)	Err.##	T (°)	P (°)	Err.	T (°)	P (°)
Eastern Cordillera																								
EC1	65.47	17.64	159	1	55	Osb	1.07	1	0.93	0.10	0.01	0.00	0.9	0.3	0.2	25	13	4	118	15	5	256	70	3
EC2	65.58	17.67	112	10	55	Osb	1.10	1	0.89	0.07	0.01	0.01	0.8	0.3	0.2	275	6	3	182	21	3	19	68	2
EC3	65.46	17.49	287	54	55	Osb	1.05	1	0.94	0.14	0.00	0.00	0.8	0.1	0.1	167	42	5	61	17	5	315	43	3
EC4	65.34	17.91	97	10	55	Osb	1.09	1	0.89	0.06	0.02	0.01	0.8	0.3	0.1	89	25	4	201	39	4	336	41	2
EC5	65.38	17.98	337	40	55	Osb	1.04	1	0.91	0.06	0.00	0.01	0.4	0.0	0.4	109	5	89	200	11	89	352	78	4
EC6	65.21	18.24	225	12	72	Su	1.08	1	0.93	0.08	0.00	0.03	1.1	0.1	1.1	252	21	21	356	31	23	134	51	14
EC7	65.18	18.24	167	12	72	Osb	1.06	1	0.87	0.11	0.02	0.00	0.4	0.1	0.0	292	22	38	197	13	38	80	64	5
EC8	65.25	18.36	182	55	72	Osb	1.06	1	0.88	0.06	0.01	0.00	0.5	0.1	0.0	279	6	7	189	2	7	81	84	1
EC9	65.20	18.42	190	62	72	Sc	1.02	1	0.96	0.08	0.02	0.01	0.6	0.9	0.5	106	28	90	220	37	90	349	40	26
EC10	65.23	18.42	188	15	72	Osb	1.11	1	0.97	0.03	0.00	0.01	3.6	0.0	3.1	124	32	33	32	2	37	299	58	20
EC11	65.24	18.43	162	68	72	Osb	1.06	1	0.90	0.10	0.00	0.01	0.5	0.0	0.5	274	3	90	184	4	90	43	85	2
EC12	65.26	18.29	310	33	55	Osb	1.12	1	0.88	0.06	0.01	0.00	0.8	0.0	0.0	120	19	20	221	28	20	0	55	6
EC13	65.28	18.27	331	52	55	Osb	1.06	1	0.90	0.06	0.01	0.00	0.5	0.7	0.0	162	42	6	262	10	8	3	46	7
EC14	65.34	18.20	312	55	55	Osb	1.06	1	0.91	0.08	0.01	0.02	0.6	0.2	0.6	265	4	18	174	20	18	5	70	2
EC15	65.45	18.09	312	66	55	Sc	1.14	1	0.94	0.05	0.00	0.05	2.4	0.0	2.2	86	7	85	355	10	84	209	78	9
EC16	65.49	18.02	31	14	55	Dv	1.06	1	0.90	0.05	0.00	0.01	0.5	0.0	0.5	56	7	87	146	6	87	275	81	3
EC17	65.51	18.06	69	16	55	Osb	1.04	1	0.85	0.03	0.01	0.01	0.2	0.1	0.1	301	7	21	207	27	21	45	62	2
EC18	65.53	18.07	288	56	55	Osb	1.12	1	0.94	0.06	0.03	0.00	1.8	0.4	0.5	228	19	20	132	17	23	2	64	12
EC19	65.53	18.07	297	51	55	Osb	1.10	1	0.92	0.04	0.01	0.00	1.2	0.0	0.4	119	28	17	23	12	18	272	60	7
EC20	65.87	17.81	140	29	55	Osb	1.03	1	0.90	0.05	0.01	0.00	0.3	0.4	0.0	70	3	33	339	10	33	177	79	3
EC21	65.86	17.50	85	38	55	Osb	1.02	1	0.81	0.13	0.03	0.02	0.1	0.2	0.1	319	25	34	60	21	34	184	57	4
EC22	66.31	17.28	162	35	55	Oa	1.01	1	0.85	0.07	0.04	0.04	0.1	0.0	0.1	278	19	71	187	2	71	92	71	4
EC23	66.35	17.58	125	32	55	O	1.15	1	0.99	0.10	0.00	0.05	10.2	0.0	9.2	235	3	50	325	12	49	132	78	9
EC24	65.91	18.11	128	39	55	Osb	1.06	1	0.91	0.05	0.01	0.01	0.6	0.0	0.6	115	1	37	25	43	35	206	47	13
EC25	66.05	18.03	322	70	55	Oa	1.11	1	0.94	0.08	0.00	0.01	1.8	1.9	0.0	285	8	28	23	43	25	187	46	14
EC26	66.49	18.45	158	69	55	Sl	1.06	1	0.94	0.05	0.00	0.00	1.0	0.7	0.0	132	2	52	41	34	49	225	56	16
EC27	67.00	18.39	347	36	86	Sl	1.18	1	0.94	0.07	0.00	0.04	3.1	0.9	0.0	303	2	64	200	79	20	33	11	61
EC28	68.94	15.18	264	57	55	Ou	1.08	1	0.92	0.06	0.01	0.01	0.9	0.7	0.0	251	19	11	143	42	10	360	42	7

*Sect. T: section trend.
 †Unit abbreviations are as follows: C—Carboniferous, Du—Upper Devonian, Dv—Devonian Vila Vila Formation, Sc—Silurian Catavi Formation, Si—Silurian Llagueta Formation, Su—Silurian Uncia Formation, Osb—Ordovician San Benito Formation, Oa—Ordovician Anzaldo Formation.
 ‡Mean error is the total misfit between two-dimensional (2-D) ellipses and best-fit 3-D ellipsoid (see Mookerjee and Nickleach, 2011).
 §ε_s is the octahedral shear strain, or average natural strain, represented by the 3-D ellipsoid.
 **Flinn's k is the ratio of R_{xy} to R_{yz}; k > 1.0 represents prolate ellipsoids (R_{xy} > R_{yz}), and k < 1.0 represents oblate ellipsoids (R_{xy} < R_{yz}).
 ††T—trend.
 ‡‡P—plunge.
 §§Err.—Angular error.

mean regional trend/plunge and error ellipse of 346/81° ± 8°/11°. Note that the Bingham axial distributions for both the in situ and restored principal axis orientations overlap within uncertainty (compare Figs. 9A and 9B).

Samples from the Subandes and Interandean zone represent Ordovician through Carboniferous stratigraphy (Fig. 3) from a wide range of structural positions within the orocline axis (Fig. 4). The in situ Interandean zone and Subandes strain ellipsoid orientations show no discernible alignment with respect to regional structural trends or sample orientation (Fig. 10A). Restoring the samples to bedding-horizontal shows that the X axes have low plunges and lie largely within the bedding plane (mean axial orientation T: 084°, P: 3°), while the Z axes are nearly perpendicular to bedding (mean axial orientation T: 342°, P: 82°; Fig. 9B). The angular errors associated with the X-axis orientations are significantly higher (between ±10° and 90°) compared to the Z axes (maximum ±30°; Fig. 10C). Ellipsoids projected onto the balanced cross section have bedding-perpendicular Z axes and bedding-parallel X axes regardless of thrust sheet location or position with respect to fold axes and adjacent faults (Fig. 11). These ellipsoid orientations are equally consistent with a sedimentary fabric or a weak, vertical compressive stress field related to compaction. Regardless, this indicates that regionally significant, granular shortening was not accommodated in the Subandes or Interandean zone.

Eastern Cordillera strain measurements cover Ordovician through Devonian stratigraphy (Fig. 3). As is the case in the Interandean zone and Subandes, in situ Eastern Cordillera ellipsoid axial orientations show no alignment with sample orientation or regional structural trend (Fig. 12A). Restoring the samples to bedding-horizontal results in best-fit ellipsoids with X axes that are largely within the bedding plane (mean axial orientation T: 100°, P: 1°, ±9/±16) and Z axes that range from oblique to perpendicular to bedding (mean axial orientation T: 352°, P: 81°, ±9/±16; Fig. 12B). The best-fit X and Y axial orientations have large uncertainties relative to Z axes (Table 1; Fig. 11C) due to the similar X and Y axial lengths in oblate ellipsoids (Flinn's k < 1.0, X = Y > Z). This results in large X and Y axial orientation variations during the Monte Carlo error estimation process and produces a best-fit ellipsoid with X and Y axial uncertainties that describe a common plane (Mookerjee and Nickleach, 2011). Regardless, the strain ellipsoids from the Eastern Cordillera are characterized by Z axes that range from oblique to perpendicular to bedding and Y and X axes that are coplanar within uncertainty but parallel to bedding (Fig. 13). The Eastern Cor-

TABLE 2. TWO-DIMENSIONAL (2-D) STRAIN DATA

Sample	Latitude (°S)	Longitude (°W)	Unit	2-D section	$\theta \pm 2\sigma$	$R_{\phi} \pm 2\sigma$
Interandean zone						
Bol09-145	17.88	64.6	Dv	A	7 ± 13	1.10 ± 0.02
				B	-22 ± 4	1.17 ± 0.02
Bol09-307	18.07	64.92	C	A	1 ± 7	1.13 ± 0.02
Bol09-303A	18.03	64.95	D	A	5 ± 5	1.11 ± 0.02
Bol09-278	17.83	65.09	Dv	A	16 ± 4	1.13 ± 0.02
				B	3 ± 7	1.10 ± 0.02
Bol09-257	17.8	65.1	Sc	A	-39 ± 45	1.03 ± 0.01
Bol10-3	18.25	65.22	Sc	B	41 ± 49	1.05 ± 0.02
				C	2 ± 5	1.18 ± 0.02
Bol09-80	17.64	65.2	OsB	A	19 ± 34	1.08 ± 0.02
				C	28 ± 18	1.06 ± 0.02
Bol09-49	17.78	65.27	Sc	A	7 ± 22	1.14 ± 0.02
				C	-34 ± 20	1.08 ± 0.02
Eastern Cordillera						
Bol09-322	18.17	65.13	O	A	9 ± 4	1.14 ± 0.02
Bol09-334	18.5	65.22	Dv	A	21 ± 4	1.15 ± 0.02
Bol09-396	17.6	65.3	OsB	A	-33 ± 30	1.05 ± 0.02
Bol10-38	18.12	65.42	OsB	B	19 ± 20	1.04 ± 0.02
				C	14 ± 4	1.18 ± 0.03
Bol10-41	18.09	65.43	K	A	-33 ± 13	1.12 ± 0.02
Bol10-48	18.05	65.45	S	A	-17 ± 7	1.12 ± 0.02
				C	2 ± 18	1.06 ± 0.03
Bol10-46	18.06	65.47	K	B	-27 ± 15	1.06 ± 0.02
				C	14 ± 22	1.04 ± 0.02
Bol11-180	18.01	65.5	Dv	A	-8 ± 3	1.23 ± 0.02
				B	-13 ± 7	1.12 ± 0.02
Bol10-63	18.12	65.55	OsB	A	21 ± 3	1.27 ± 0.02
				B	-21 ± 7	1.09 ± 0.02
Bol09-1	17.5	65.8	OsB	B	38 ± 29	1.07 ± 0.03
				C	-27 ± 23	1.05 ± 0.02
Bol09-428	17.53	66.09	Sc	A	-20 ± 12	1.08 ± 0.02
				B	5 ± 5	1.13 ± 0.02
Bol11-236	17.67	66.43	Sc	A	-1 ± 3	1.21 ± 0.02
Bol11-241	17.66	67	Sc	A	-12 ± 2	1.33 ± 0.02
				B	-20 ± 2	1.26 ± 0.02
Bol10-178	18.09	66.15	Oa	B	-21 ± 7	1.11 ± 0.02

Note: Unit abbreviations are as follows: C—Carboniferous, D—Devonian, Dv—Devonian Vila Vila Formation, Sc—Silurian Catavi Formation, Sl—Silurian Llallagua Formation, Su—Silurian Uncia Formation, OsB—Ordovician San Benito Formation, Oa—Ordovician Anzaldo Formation, O—Ordovician, S—Silurian, K—Cretaceous.

dillera ellipsoid orientations are consistent with either a sedimentary- or compaction-related fabric, but, at a minimum, they do not support regionally significant granular shortening.

Strain Magnitude

All of the ellipsoids showed uniformly small strain magnitudes of $\epsilon_s < 0.20$ (Fig. 3; Table 1). Most samples have ϵ_s ranging from 0.10 to 0.15, while the larger outliers range from 0.16 to 0.19. For the entire study area, the mean ϵ_s is 0.12; by physiographic region, the mean ϵ_s is 0.12 ($n = 29$) in the Eastern Cordillera, 0.11 ($n = 21$) in the Interandean zone, and 0.13 ($n = 4$) in the Subandes (Table 3). Given the dominance of sub-vertical Z axes, projecting the 3-D ellipsoids on to the cross-sectional plane roughly corresponds to either the X - Z or Y - Z strain plane and the X - Y strain plane in map view. On the cross-section plane, the 3-D ϵ_s values correspond to 2-D axial ratios of $R_{XZ/YZ} = 1.03$ – 1.23 in the Subandes and Interandean zone (Fig. 11) and $R_{XZ/YZ} = 1.05$ – 1.18 in the Eastern Cordillera (Fig. 13). The map view R_{XY} values range from 1.18 to

1.01 in the Subandes and Interandean zone and from 1.01 to 1.30 in the Eastern Cordillera (Fig. 14). The low apparent strain magnitudes and ellipsoid orientations reflect either detrital grain shapes that do not measure orogenic strain, or, at the very most, they measure a compaction strain unrelated to orogenic deformation.

Strain Ellipsoid Shape (Flinn's k Value)

The results presented herein show that the strain ellipsoid pattern at the orocline axis is characterized by Z axes perpendicular to bedding and X axes parallel to bedding. We use Flinn's k value (Flinn, 1962) to further differentiate between ellipsoid geometries dominated by greater apparent strain along X axes (R_{XY}) versus those with greater strain along the Z axes (R_{YZ}). Prolate ellipsoids have k values > 1 , due to greater X -axis extension than Z -axis compression ($R_{XY} > R_{YZ}$). Oblate ellipsoids have k values < 1 , due to greater X -axis extension than Z -axis compression ($R_{XY} < R_{YZ}$). Best-fit k values, ϵ_s , and their respective uncertainties are plotted on Flinn diagrams to interpret the dominant strain

state for each physiographic zone (Fig. 15). Since the orocline axis is dominated by ellipsoids with vertical Z axes, cases where the Z axis is not vertical are represented by squares in Figure 15. With few exceptions, oblate ellipsoids make up the majority of ellipsoid shapes. This means that any apparent strain indicated by the best-fit ellipsoids is the result of R_{YZ} strains along bedding-perpendicular Z axes and bed-parallel Y axes. By implication, the dominance of oblate ellipsoids with long dimensions parallel to bedding is consistent with a detrital fabric that records no grain-scale orogenic strain. There are few prolate ellipsoids, but the uniformly low apparent strains and high R_{ϕ} - ϕ data variability indicate that even these best-fit ellipsoids reflect detrital grain shapes rather than local orogenic strain.

DISCUSSION

Strain Pattern at the Orocline Axis

Grain shape data from competent lithologies in the central Andean orocline indicate uniformly low finite strain magnitudes. This shows that grain-scale shortening of these units has not been a significant factor in deformation of the Andean stratigraphic succession at this latitude. At both the outcrop and thin-section scale, there is a conspicuous lack of penetrative strain fabrics commonly associated with layer-parallel shortening. Micrographs and R_{ϕ} - ϕ data (Figs. 7 and 8) demonstrate that granular geometry and orientation are highly variable and strongly influenced by initial detrital grain shapes. This is conceptually consistent with the low apparent strains measured by the Fry method. Both methods produce 2-D ellipses with X axes approximately parallel to bedding.

The variability in the R_{ϕ} - ϕ data calls into question the reliability of the best-fit 3-D ellipsoids as a strain indicator, especially those with low ellipticities. Even samples with relatively larger strains ($\epsilon_s = 0.10$ – 0.20 , corresponding to a triple axial ratio range of 1.03:1:0.90–1.02:1:0.81) are characterized by apparent flattened oblate 3-D ellipsoids (k -value < 1.0 ; Fig. 15) oriented with X and Y axes parallel to bedding (Fig. 9). Only five samples (SA1, IA5, IA11, IA13, IA15; Figs. 10 and 13) have bedding-oblique Z axes ($P = 26^\circ$ – 42°), but their R_{ϕ} - ϕ data (Fig. 6) show some of the largest ϕ fluctuations ($F > 160^\circ$) and angular uncertainties (both 2-D and 3-D) of the entire data set, indicative of high detrital grain shape influence on the best-fit ellipsoids. The bedding-parallel oblate ellipsoids may be consistent with a compaction strain fabric acquired during lithification, but it is equally likely they reflect depositional grain orientations. Likewise,

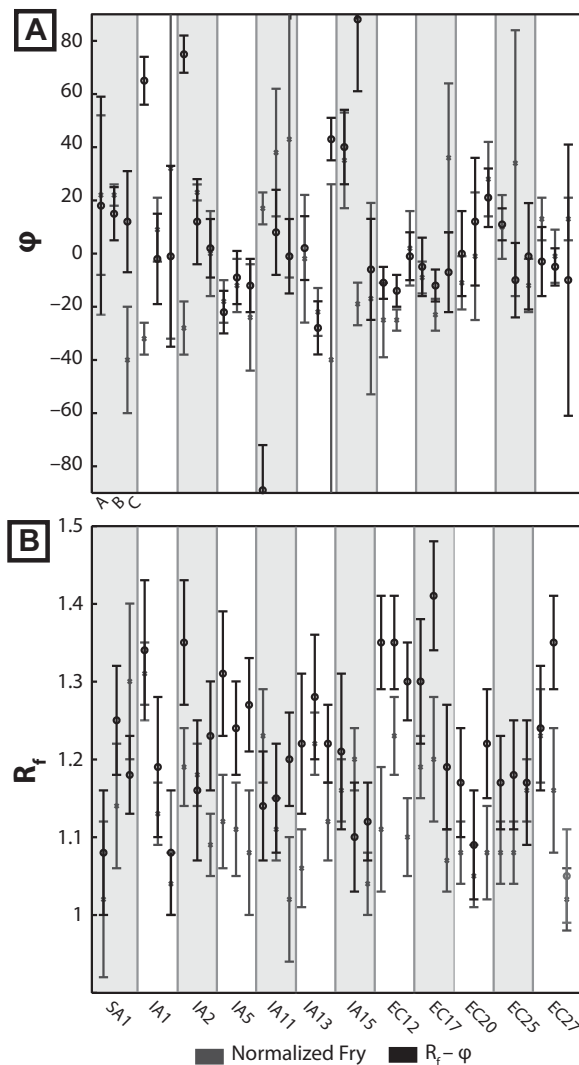


Figure 7. Comparison of Fry and R_f - ϕ best-fit two-dimensional (2-D) ellipse parameters and 2σ uncertainties: (A) best-fit ϕ , relative to bedding ($\phi = 0$) and (B) best-fit axial ratios, R_f . The results are plotted from east to west and alphabetically for each sample: strike parallel (A-cuts), dip parallel (B-cuts), and bedding parallel (C-cuts).

the degree of grain shape variability present in the bedding-oblique prolate ellipsoid samples indicates that they never accommodated sufficient granular strain to attain even weak anisotropic granular distributions and orientations. Even if the ellipsoids for all the samples presented here merely measure detrital grain shapes, they rule out significant granular shortening parallel to bedding in the region.

One of the primary motivations for quantifying grain-scale shortening in the central Andes is to assure an accurate assessment of total crustal shortening and material displacement during orocline formation. The lack of granular strain and layer-parallel shortening at the orocline axis means that out-of-plane strain is negligible, and shortening estimates from balanced cross sections do not ignore additional grain-scale shortening. As a result, the out-of-plane motion required by the continuing evolution of the Bolivian orocline as a secondary arc

must be largely accommodated by out-of-plane displacement in map-scale structures rather than out-of-plane strain at a granular scale. Orogen-parallel displacements have been documented along strike-slip and transpressional structures such as the Cochabamba and Rio Novillero fault zones (Dewey and Lamb, 1992; Kley, 1999; Eichelberger et al., 2013).

Deformation Conditions in the Central Andes

Compared to other orogens where internal strain is well documented in competent, grain-supported rocks, the central Andes are exceptional in the apparent lack of significant grain-scale shortening. We suggest that both temperature and lithologic conditions in the central Andes inhibited the microscale deformation mechanisms that accommodate layer-parallel shortening. CL images indicate

that grains have cement overgrowths rather than the sutured grain boundaries associated with dynamic recrystallization (Fig. 5B). The absence of microstructural evidence for dynamic recrystallization (Poirier et al., 1979) in the samples presented here is consistent with the low-strain-magnitude measurements. Since dynamic recrystallization is largely temperature dependent, internal strain accumulation in the central Andes may have been limited by low-temperature conditions that prevented strain accommodation by dislocation creep (i.e., Hirth and Tullis, 1992). The lack of dynamic recrystallization textures even at the base of the central Andean stratigraphic section implies deformation occurred at temperatures below the frictional-viscous transition for quartz (Schmid and Handy, 1991). The temperature threshold estimates for grain-boundary migration processes range from 250 ± 20 °C to as high as 310 ± 30 °C (Voll, 1976; Dunlap et al., 1997; van Daalen et al., 1999; Stöckhert et al., 1999; Stipp et al., 2002). For the southern limb of the central Andean orocline, unreset zircon fission-track (ZFT) ages (ca. 385–481 Ma) from Ordovician, Silurian, and Devonian stratigraphy (Barnes et al., 2008) limit deformation temperatures to $<240 \pm 10$ °C (based on the annealing temperature for zircon; Brandon et al., 1998; Fig. 16A). At the orocline axis, unreset zircon (U-Th)/He (ZHe) ages (459 Ma and 475 Ma) from Upper Devonian stratigraphy in the Subandes (Eichelberger et al., 2013) further constrain deformation temperatures to <160 – 200 °C (Fig. 16A; Reiners et al., 2004). Based on these constraints, temperature conditions were too low for significant quartz crystal-plastic deformation.

The lower temperatures at the orocline axis and southern limb may be partly due to the amount of synorogenic sedimentation and burial of the developing fold-and-thrust belt. Tertiary synorogenic sediments preserved in Subandean synclines range from ~5–7 km in the northern limb (Baby et al., 1995; Watts et al., 1995) to ~2–4 km in the southern limb (Dunn et al., 1995; Baby et al., 1995). These sediments are barely preserved in the Subandes at the orocline axis, where the modern foredeep containing Tertiary and younger sediments is only 1.5–2 km (Moretti et al., 1996). Exhumation magnitudes estimated from thermochronology in the Bolivian Andes increase from the Subandes westward to the Eastern Cordillera, ranging from 3 km to 11 km in the north limb (Barnes et al., 2006; McQuarrie et al., 2008), 3 km to at least 6 km at the orocline core (Barnes et al., 2012; Eichelberger et al., 2013), and <4 km to 7 km in the south limb (Barnes et al., 2008). For the study area at the orocline

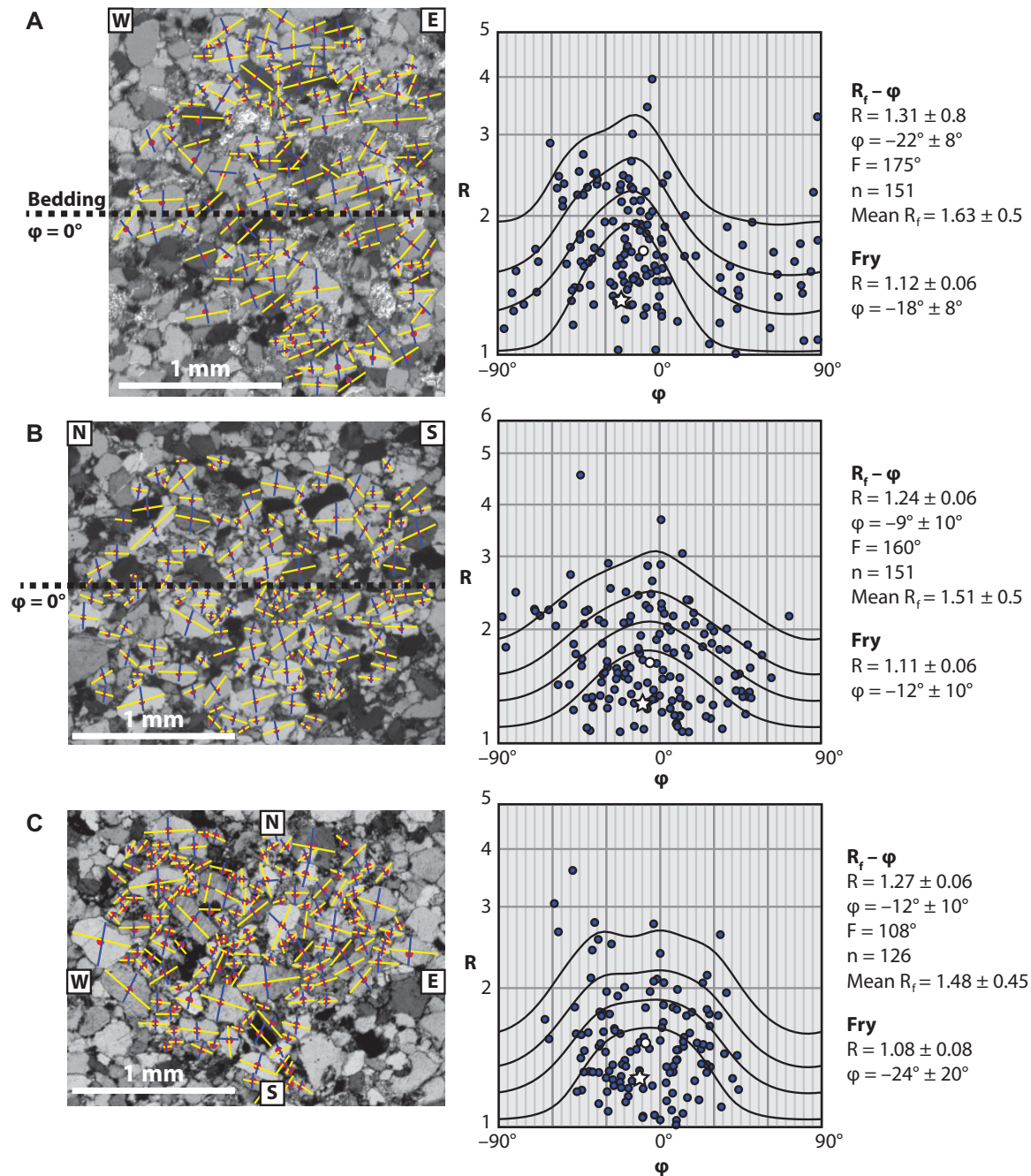


Figure 8. Example of R_f - ϕ data from the A (dip direction parallel), B (strike direction parallel), and C (bedding parallel) planes for sample IA5. The cardinal orientations of each micrograph are shown in the corners of each image. For A and B, micrographs are oriented parallel to bedding. R_f - ϕ plots are ϕ versus $\ln(R_f)$ with $\phi = 0$ indicating bedding-parallel long axes. Contours are cumulative probability density, white star is best-fit ellipse, and white circle is mean ellipse shape. Best-fit R (axial ratio) and ϕ (long-axis angle from horizontal) with 2σ uncertainties are listed at right. F is fluctuation of ϕ angles; n is number of grains measured. R_f - ϕ plots, contours, and best-fit R_f - ϕ parameters were produced using EllipseFit (Vollmer, 2011a).

core, even the most deeply exhumed samples record minor strain. Additionally, samples SA3 and SA4 come from the northern limb Subandes, where synorogenic sediments are thicker than the orocline axis, yet they still indicate negligible strain. It is possible that rocks

exposed in the northern limb Eastern Cordillera may exhibit greater strain, since they were exhumed from greater depths and experienced higher temperatures (Barnes et al., 2006, and references therein) than rocks from the orocline axis where the strain data were collected.

Layer-Parallel Shortening Accommodation at Low Temperatures

In thrust sheets where deformation temperatures exceeded the $\sim 270^\circ\text{C}$ threshold for dislocation creep and dynamic recrystallization,

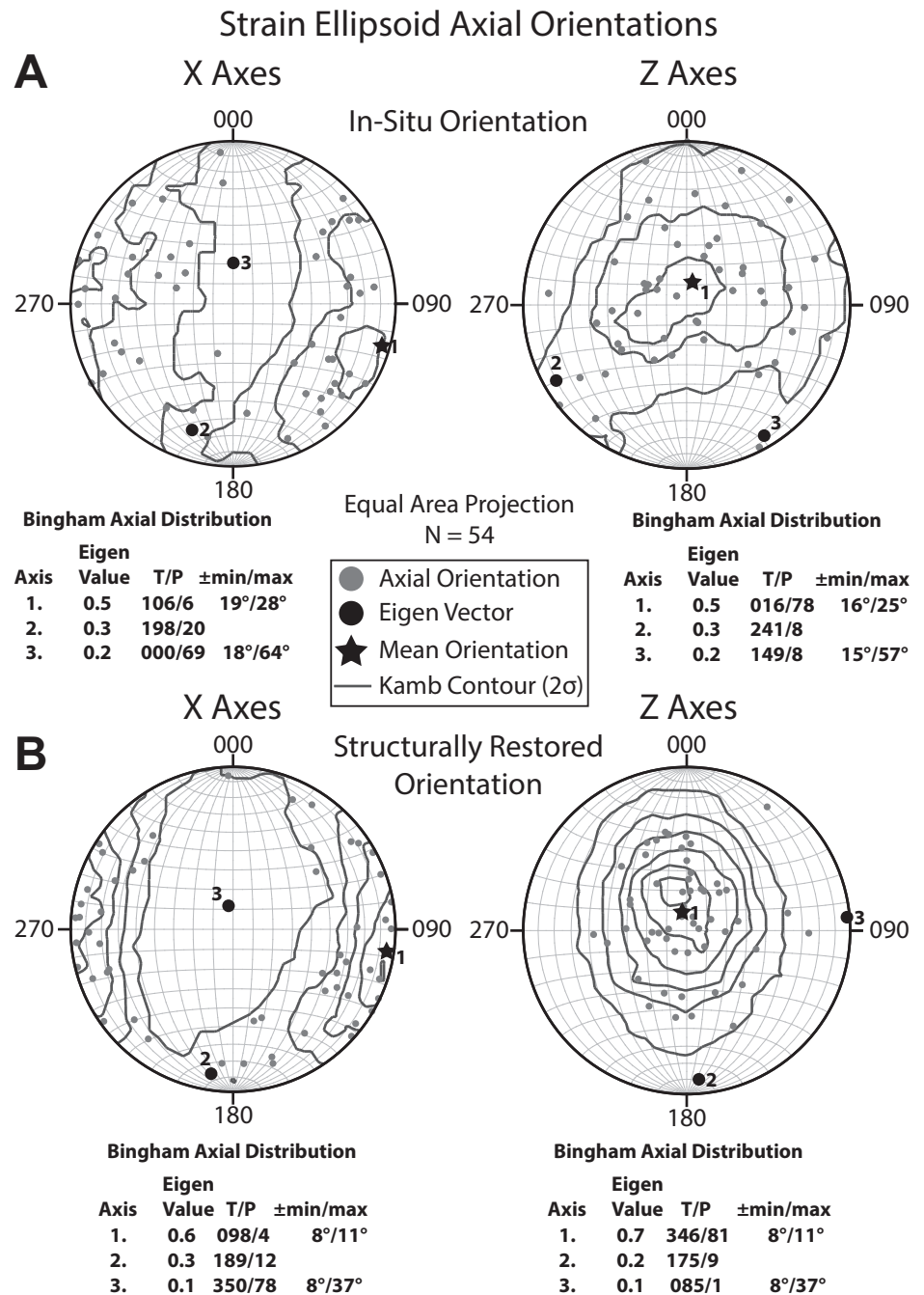


Figure 9. (A) In situ three-dimensional (3-D) finite strain ellipse X- and Z-axial orientations and (B) axial orientations after restoring bedding at the sample location to horizontal. Gray points are axial orientations, gray lines are Kamb contours at 2σ intervals, and black numbered poles are Bingham axial distribution eigenvectors. Normalized eigenvalues, orientations, and uncertainties are listed for each data set. The largest eigenvalue reflects the region of highest point density and is interpreted as the mean axial orientation. The lowest eigenvector indicates the region of lowest point density. Plots and Bingham axial distributions were produced using Stereonet 8 (Allmendinger et al., 2013; Cardozo and Allmendinger, 2013).

large coaxial strains are commonly observed in grain-supported lithologies ($R_s > 1.5$; Fig. 16A; Yonkee, 2005; Long et al., 2011). The absence of similar strain in the central Andes is easily linked to deformation temperatures $< 230^\circ\text{C}$. However, the factors responsible for limited layer-parallel shortening in the central Andes and the minor contribution of grain-scale shortening to the total shortening budget are more complex. In other fold-and-thrust belts, grain-supported lithologies record granular layer-parallel shortening at temperatures $< 300^\circ\text{C}$

(e.g., Yonkee and Weil, 2010; Sak et al., 2012). The Pennsylvania salient of the Appalachian fold-and-thrust belt and the Sevier thrust belt both have greater regional layer-parallel shortening than the central Andes, but deformation temperatures are similar to slightly higher. In Bhutan, minor layer-parallel shortening ($\sim 7\%$) is limited to external thrusts where minimum deformation temperatures were definitively higher, exceeding $> 160\text{--}200^\circ\text{C}$ based on reset ZHe ages (Long et al., 2011, 2012). In the central Andes, strains are at or below the limit of

reasonable detection, with deformation temperatures of $< 230^\circ\text{C}$ to as low as $< 180^\circ\text{C}$ (Table 4; Fig. 16A; Barnes et al., 2008; Eichelberger et al., 2013). This temperature range is comparable to the Appalachian and Sevier thrust belts at the shallowest levels, suggesting the factors limiting layer-parallel shortening in the central Andes are more nuanced. In addition to temperature, factors such as lithologic composition and mechanical stratigraphy also appear to influence internal strain development at temperatures below $\sim 200^\circ\text{C}$.

Subandean and Interandean Zone Axial Orientation

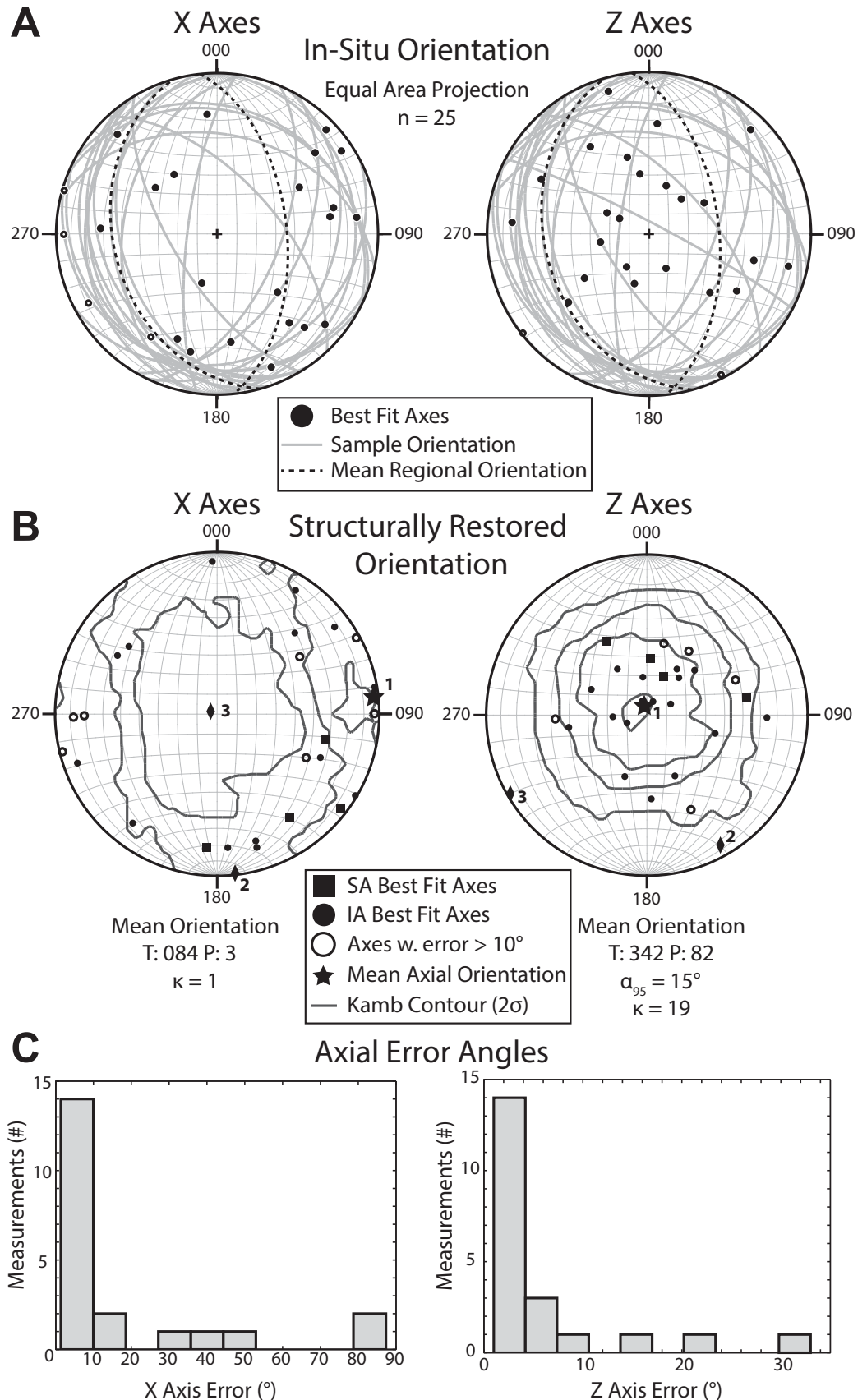


Figure 10. Orientation of *X* and *Z* axes of finite strain ellipsoids from the Subandes (SA, square) and Interandean zone (IA, circles). (A) In situ axial orientations with sample bedding orientation (gray lines) and mean regional bedding orientation (dashed black line). (B) Axial data after bedding is structurally restored to horizontal by rotation around bedding trend. Numbered points are Bingham axial distribution eigenvectors with the largest eigenvector (1) interpreted to be the mean axial orientation, plotted as a star. Samples with best-fit ellipsoid axial angular errors greater than 10° are indicated by hollow markers. (C) Histograms indicate that the majority of samples have axial errors less than 10°. Note the difference in the error angle scale between the horizontal axes.

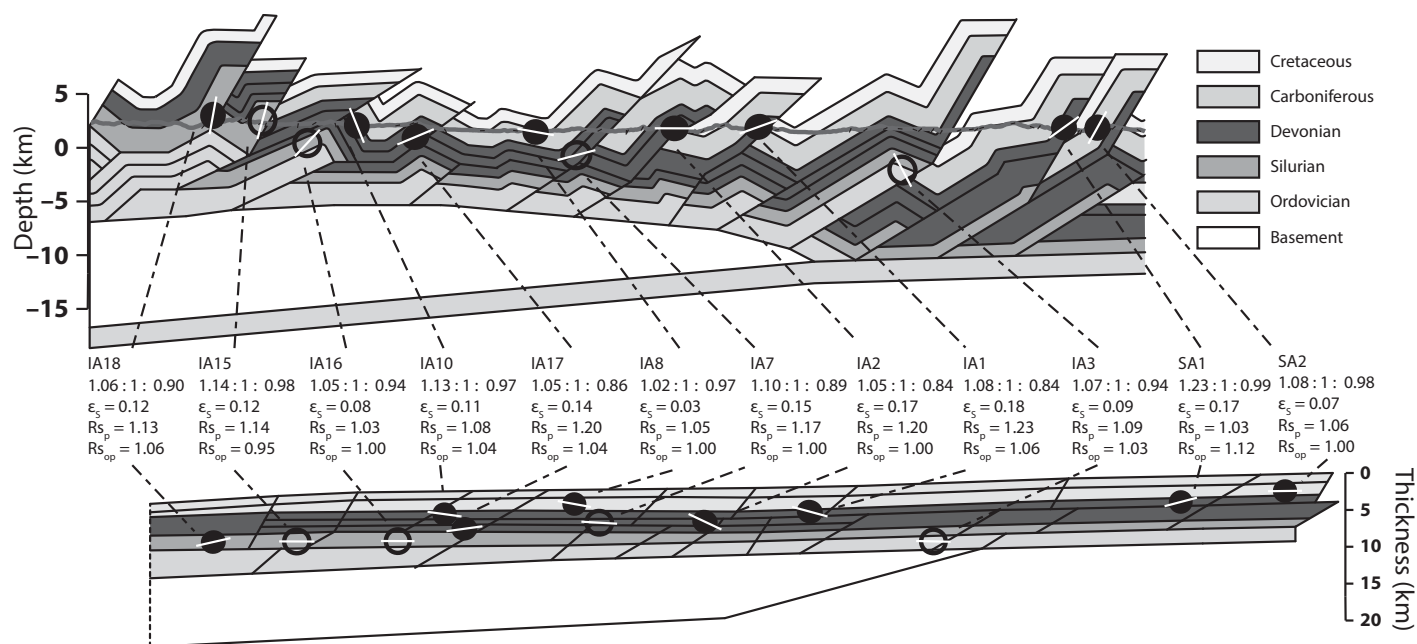


Figure 11. Balanced cross section from Eichelberger et al. (2013) showing structural context of Subandean and Interandean zone samples. Ellipses are the projection of the three-dimensional (3-D) ellipsoid onto the cross-section plane. (Top) Deformed section shows in situ orientation of best-fit ellipsoids with long axis shown in white. Hollow markers indicate samples projected from north of the line of section where deeper stratigraphy is exposed than along the line of section. (Bottom) Structurally restored section with ellipses in restored orientation. For each sample, the following strain parameters are listed: the triple axial ratio (X:Y:Z), octahedral shear strain (ϵ_s), axial ratio in the plane of section (R_p), and axial ratio out of the plane of section (R_{op}).

Sevier Belt Deformation Conditions and Mechanical Stratigraphy

The Wyoming salient in the Sevier fold-and-thrust belt of the western United States has accommodated up to 30% layer-parallel shortening, depending on structural location (Crosby, 1969; Gockley, 1985; Craddock, 1992; Mitra, 1994; McNaught and Mitra, 1996; Mukul and Mitra, 1998; Yonkee, 2005; Yonkee and Weil, 2010). In the Sevier fold-and-thrust belt, layer-parallel shortening is best defined in the Jurassic Twin Creek (argillaceous micritic limestone; Imlay, 1967) and Triassic Ankareh (quartzose to arkosic sandstone and mudstone; Kummel, 1954) Formations (e.g., Mitra, 1994; Yonkee and Weil, 2010; Weil and Yonkee, 2012). Despite the apparent lithologic competency contrast between the matrix-supported Twin Creek and the grain-supported Ankareh Formations, both formations record roughly equivalent strain orientations and magnitudes (see Yonkee and Weil, 2010). These units are directly below the Jurassic through Cretaceous synorogenic sediment load deposited during Sevier deformation, which reached thicknesses of ~3–5 km (Yonkee et al., 1997; DeCelles and Coogan, 2006), comparable to synorogenic sediment thicknesses in the central Andes. Reset AFT ages from the Jurassic Stump, Triassic Nugget, and Permian

Weber Formations demonstrate deformation temperatures exceeded ~100–120 °C where layer-parallel shortening is documented in the frontal thrust systems of the Sevier thrust belt (Fig. 16A; Burtner and Nigrini, 1994). This corresponds to minimum exhumation magnitudes comparable to the central Andes (~4–5 km), suggesting similar magnitudes of burial for formations where layer-parallel shortening is documented in the Sevier belt.

From east to west, the major thrusts of the Sevier system are the Prospect, Hogsback, Absaroka, Darby, Crawford, and Meade thrusts (Armstrong and Oriol, 1965; Royse et al., 1975; Coogan, 1992; Yonkee et al., 1997). Illite crystallinity data from cleavage seam materials and thermal modeling estimated maximum temperatures of ~190 °C for the Twin Creek Formation in the Prospect thrust, ~140 °C in the Absaroka thrust, and ~210 °C in the Crawford thrust (Mitra and Yonkee, 1985). Fluid inclusion entrapment temperature estimates from the Twin Creek Formation in the Darby thrust sheet at the Absaroka footwall range from 175 °C to 328 °C (Wiltshko et al., 2009). The lower end of this temperature range is comparable to the Crawford, Absaroka, and Prospect thrusts (Fig. 16A), but the highest fluid inclusion temperatures probably exceed actual deformation temperatures for the Darby thrust. As discussed already, deforma-

tion temperatures over 250–300 °C would allow for plastic quartz failure and probably result in large layer-normal flattening strains (similar to Bhutan), whereas layer-parallel shortening is <10% in the Darby area (Fig. 16A; Yonkee and Weil, 2010). Overall, deformation temperatures in the Sevier thrust belt were above 130 °C and range from 175 °C to 210 °C where layer-parallel shortening is most significant, potentially exceeding maximum temperatures inferred for the central Andes.

Sevier thrust sheets with the highest cleavage intensity experienced elevated pressures and temperatures approaching ~175–210 °C due to thrust fault loading along their hinterland trailing edge (Mitra and Yonkee, 1985). For example, the Twin Creek Formation in the Crawford thrust (buried by the older Willard and Meade thrusts to the west) has high cleavage intensity, 10%–30% layer-parallel shortening, and temperatures of ~210 °C (Fig. 16A; Mitra and Yonkee, 1985; Yonkee and Weil, 2010). Stratigraphically below the Twin Creek Formation in the same thrust, the Ankareh Formation features calcite and quartz dissolution cleavage and 10%–30% layer-parallel shortening (Fig. 16A; Yonkee and Weil, 2010). Given the presence of quartz dissolution textures in the Crawford thrust, deformation temperatures of ~210 °C appear to be sufficient to activate pressure solu-

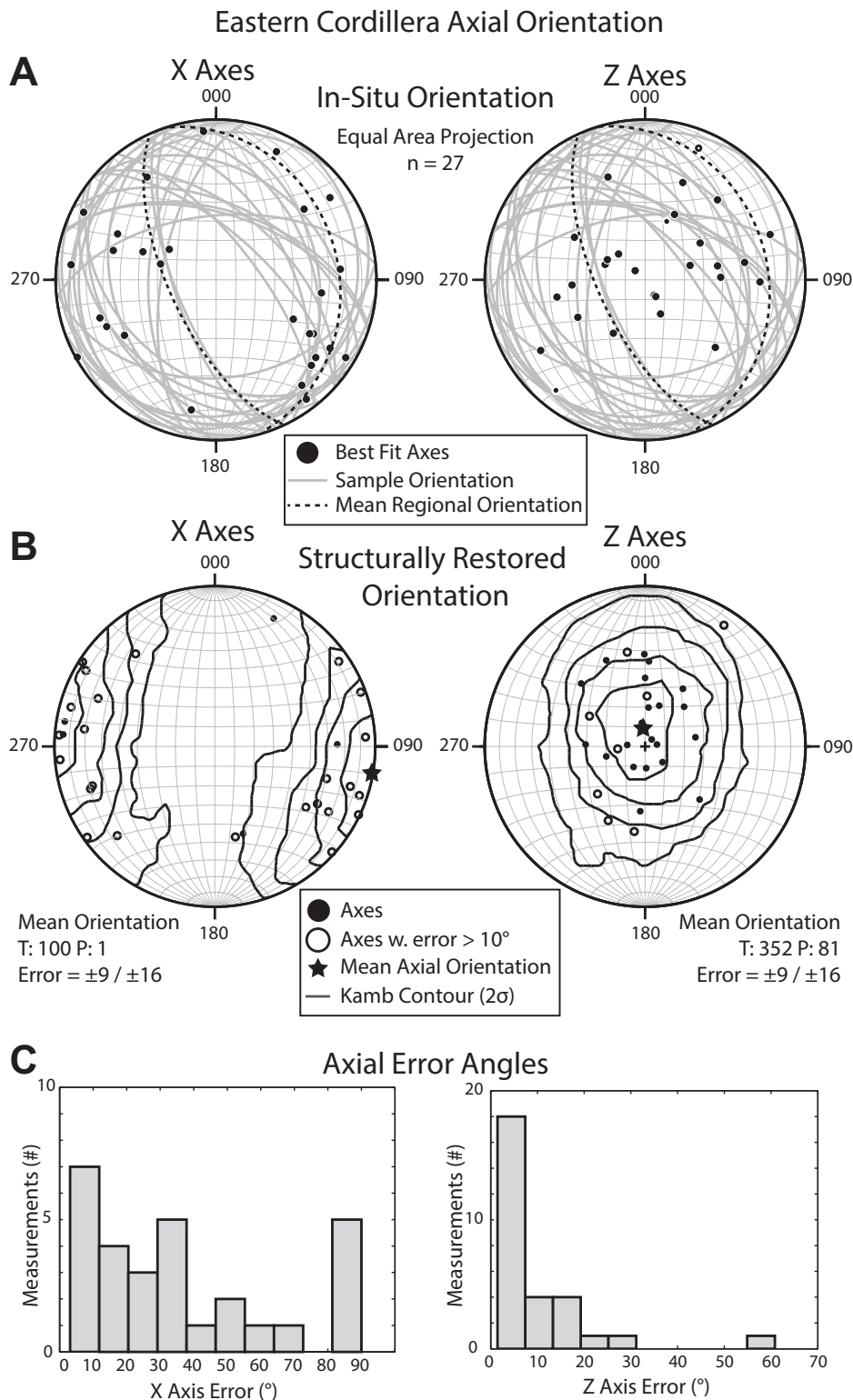


Figure 12. Orientation of X and Z axes of finite strain ellipsoids from the Eastern Cordillera. (A) In situ axial orientations with sample bedding orientation (gray lines) and mean regional bedding orientation (dashed black line). (B) Axial data after bedding is structurally restored to horizontal by rotation around bedding trend. Symbolry is the same as Figure 9. Samples with axial angular errors greater than 10° are indicated by hollow markers. (C) Histograms at the bottom indicate that the majority of samples have axial errors less than 10°. Note the difference in the error angle scale between the horizontal axes.

tion in quartz. At lower temperatures, layer-parallel shortening and cleavage are less significant: 5%–10% for the Absaroka (~140 °C) and Prospect (~180 °C) thrusts to 10% and lower for the easternmost Hogsback thrust (Fig. 16A; Mitra and Yonkee, 1985). With the exception of the Absaroka thrust, these temperatures still exceed the likely temperature range for the central Andes (Fig. 16A).

Differences in mechanical stratigraphy may help to explain the limited nature of internal strain in the central Andes versus the Sevier fold-and-thrust belt. From a structural standpoint, the Sevier thrusts act as cohesive sheets over large distances with less internal faulting or folding than seen in the central Andes. The Sevier thrusts offset 3.5–4.5-km-thick stratigraphic packages (excluding synorogenic strata) from a common detachment at ~5–7 km depth and slip distances of 15–40 km at structural wavelengths of ~20–50 km (Dixon, 1982; Coogan, 1992; Royse, 1993; Yonkee et al., 1997). The extent of the Sevier faults contributed to increased footwall pressures and temperatures, producing conditions amenable to pressure solution and layer-parallel shortening in the Crawford thrust (Mitra and Yonkee, 1985). By comparison, central Andean faults generally have <10 km of slip and are spaced ≤20 km apart (Eichelberger et al., 2013). Relative to the Sevier, thrust faults in the central Andes have much lower displacements and structural wavelengths, potentially due to the presence of six thick (≥1 km) shale sequences (Fig. 16A). These mechanically weak intervals act as detachment horizons at various stratigraphic levels, preventing slip from localizing along a single detachment, such as in the Sevier thrust belt (Fig. 16A). As a result, central Andean faults are more numerous but not laterally extensive enough to significantly increase footwall deformation temperatures over a broad area.

Composition may also be an important factor in granular shortening, especially at temperatures below ~180 °C. In particular, 5%–10% layer-parallel shortening is documented in the Absaroka thrust, but deformation temperatures (~140 °C) were similar to the central Andes (Fig. 16A). Unlike the Absaroka thrust, spaced cleavage is not pervasive in the central Andes, and microtextural evidence of pressure solution in quartz is absent. The presence of regional cleavage and layer-parallel shortening at low temperatures in the Absaroka thrust but not the Andes may stem from the prevalence of calcareous lithologies in the Sevier belt (Fig. 16A). Calcareous lithologies in Bolivia are minor and discontinuous, whereas numerous calcareous intervals that feature pervasive layer-parallel shortening are found in the Sevier belt (Fig. 16A). In the Absaroka thrust, both units record

Andean orocline strain and orogen-scale factors influencing grain-scale shortening

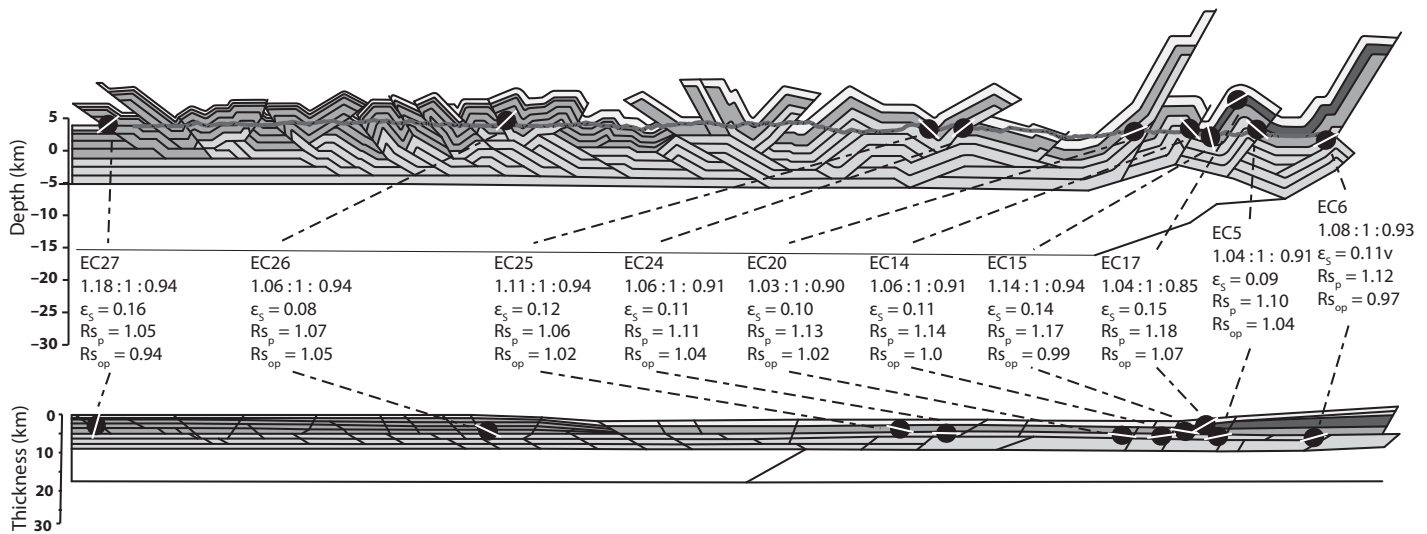


Figure 13. Balanced cross section from Eichelberger et al. (2013) showing structural context of Eastern Cordillera samples. Ellipses are the projection of the three-dimensional (3-D) ellipsoid onto the cross-section plane. (Top) Deformed section shows in situ orientation of best-fit ellipsoids with long axis shown in white. (Bottom) Structurally restored section with ellipses in restored orientation. For each sample, the following strain parameters are listed: the triple axial ratio ($X:Y:Z$), octahedral shear strain (ϵ_s), axial ratio in the plane of section (R_p), and axial ratio out of the plane of section (R_{op}). Unit shading is the same as Figure 11.

comparable magnitudes of layer-parallel shortening, but spaced cleavage is better developed in calcareous lithologies compared to the quartzose sandstone in the Ankareh Formation (Mitra, 1994; Yonkee and Weil, 2010). For temperatures between 100 °C and 200 °C and pressures on the order of 100–300 MPa, pressure solution in quartz is predicted to accommodate strain rates of $<10^{-13}$ – 10^{-15} s⁻¹, compared to 10^{-11} – 10^{-12} s⁻¹ for calcite (Rutter, 1976). Within the probable ~140 °C deformation temperature range where layer-parallel shortening is found in the Absaroka thrust, predicted strain rates for both quartz and calcite fall within the representative range for orogenic deformation (Pfiffner and Ramsay, 1982; Ramsay, 2000; van der Pluijm and Marshak, 2004). Comparable strains are measured in both calcareous and siliciclastic units in the Sevier belt; however, calcite is mechanically able to accommodate more internal strain by pressure solution under low-pressure and low-temperature conditions. The relative weakness of calcareous strata in the Sevier belt may have facilitated minor internal strain and cleavage development at temperatures <180–210 °C, whereas the absence of similar lithologies in the central Andes may have precluded cleavage development.

Appalachian Deformation Conditions

Appalachian internal strain and layer-parallel shortening magnitudes are interpreted to be stratigraphically uniform and only vary

between structural domains: 20% layer-parallel shortening in Devonian through Mississippian rocks of the Valley and Ridge and 14% layer-parallel shortening in Silurian through Mississippian rocks of the Appalachian Plateau (Nickelsen, 1963, 1983; Engelder, 1979a, 1979b; Slaughter, 1982; Geiser and Engelder, 1983; Gray and Mitra, 1993; Fail and Nickelsen, 1999; Sak et al., 2012). Strain measurements in the Pennsylvania salient region were based on crinoid ossicles in calcareous siltstone lithologies and distorted grains (Fry method) for grain-supported sandstone lithologies. As with the Sevier belt, strain results from the Appalachians are consistent between grain-supported and matrix-supported lithologies, despite any apparent competency contrast (Sak et al., 2012).

Mesozoic AFT ages indicate regional Alleghanian deformation temperatures of >100 °C across Pennsylvania (Roden et al., 1989; Roden, 1991; Blackmer et al., 1994), comparable to the central Andes, where AFT ages are regionally reset except for the Subandes in the southern limb (Barnes et al., 2008). Fluid inclusions and vitrinite reflectance data from West Virginia suggest a temperature range of 130–160 °C for Pennsylvanian strata in both the Appalachian Plateau and Valley and Ridge (Reed et al., 2005). Thermal modeling, vitrinite reflectance, and fluid inclusion data from the Pennsylvania Valley and Ridge indicate temperature conditions ranging from 160 °C to 217 °C between the Devonian Catskill and the Ordovician Martinsburg Formations (Lacazette, 1991; Evans,

TABLE 3. STRAIN RESULTS SUMMARY

	Mean ϵ_s	n	Standard deviation	X plunge (°)	Error angle (°)	Z plunge (°)	Error angle (°)	ϵ_{op}	Error
Physiographic mean									
All	0.01	54	0.04	16	12	59	16	0.01	0.04
Eastern Cordillera	0.12	29	0.03	15	12	60	17	0.01	0.04
Interandean zone	0.01	21	0.04	16	13	57	16	0.01	0.04
Subandes	0.01	4	0.04	20	11	53	14	0.03	0.06
Stratigraphic mean									
Eastern Cordillera									
Ordovician	0.12	23	0.03	16	13	62	14	0.02	0.03
Silurian	0.14	5	0.03	12	12	47	25	-0.02	0.04
Devonian	0.12	1							
Subandes and Interandean zone									
Ordovician	0.11	5	0.05	13	16	46	16	0.00	0.04
Silurian	0.11	8	0.04	13	11	61	16	0.03	0.04
Devonian	0.14	7	0.08	24	12	57	16	-0.01	0.03
Carboniferous	0.14	5	0.05	17	10	62	15	0.04	0.05

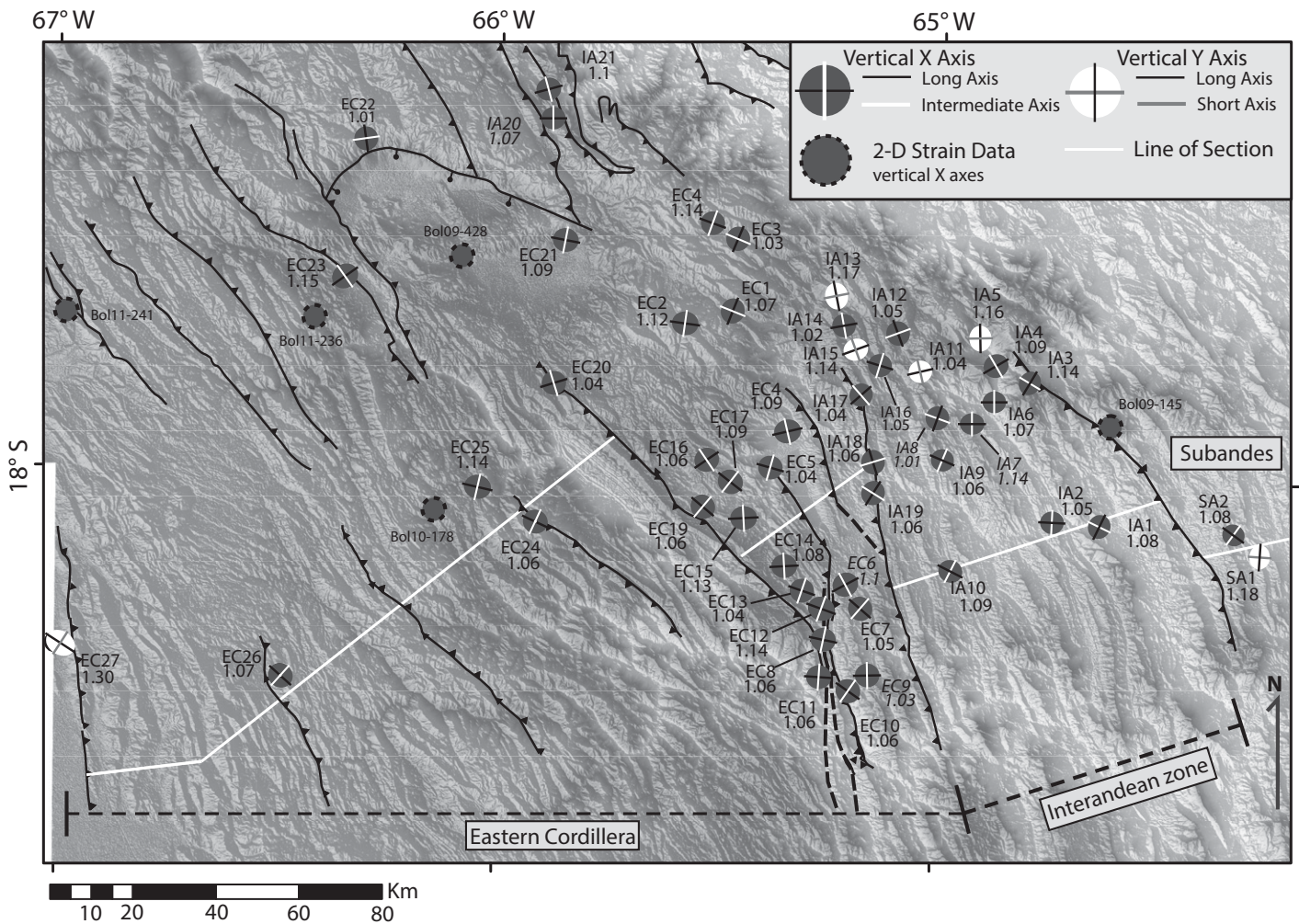


Figure 14. Advanced Spaceborne Thermal Emission and Reflection Radiometer (ASTER) 30 m digital elevation model (DEM) and geologic map with three-dimensional (3-D) ellipsoids projected onto the horizontal map-view plane. Black ellipses indicate samples with vertical short (Z) axes, and white ellipses indicate samples with vertical intermediate (Y) axes. The orientations of the remaining horizontal axes are indicated by solid lines. The R_s value of the 3-D finite ellipsoid projected into the map-view plane is listed for each sample. The locations of two-dimensional (2-D) strain data from regions with limited 3-D data coverage are shown by circles with dashed borders. Dark-gray circles indicate 2-D finite ellipsoids with vertical X axes. Geology is from McQuarrie (2002) and Eichelberger et al. (2013).

1995; Evans and Battles, 1999). Overall, Valley and Ridge deformation temperatures range from ~ 130 °C to 200 °C, but the majority of the sampled stratigraphy probably surpassed 160 °C, exceeding deformation temperatures in the central Andes (Fig. 16B). The Valley and Ridge and the Crawford thrust in the Sevier belt attained temperatures over ~ 170 °C and both accommodated 20% layer-parallel shortening (Fig. 16A; Yonkee and Weil, 2010). Thermochronologic exhumation constraints are limited for the Appalachians, but these deformation temperatures suggest exhumation magnitudes on the order of at least 6–7 km (assuming 25 °C/km geothermal gradient). Compared to the central Andes, this is at the upper end of exhumation estimates for the Eastern Cordillera, but no layer-parallel short-

ening is documented even though the depth of orogenic exposure is similar.

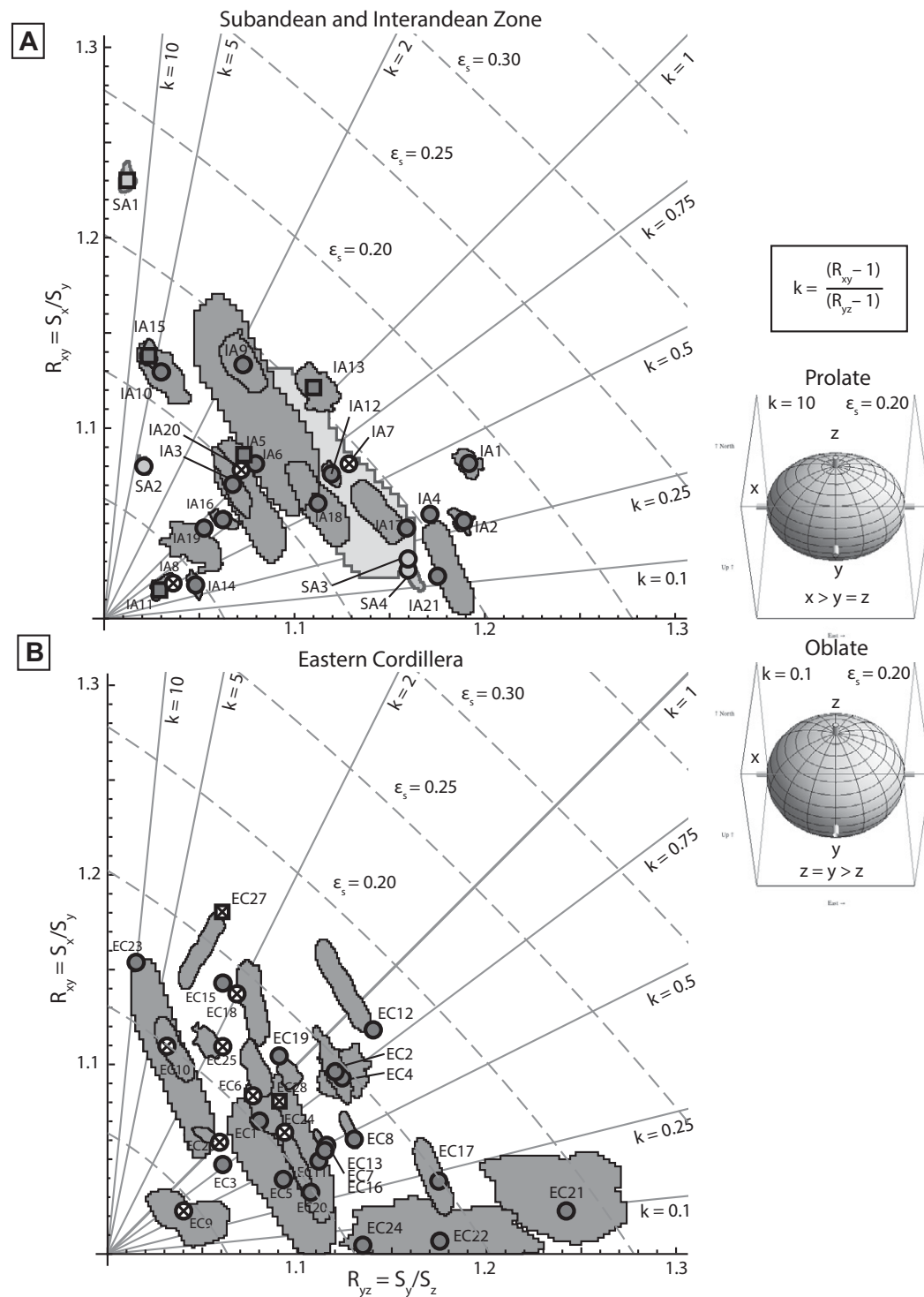
At the Allegheny Front (Valley and Ridge–Appalachian Plateau boundary), reset K-Ar ages (<400 Ma; Pierce and Armstrong, 1966) from fault mylonite in the Ordovician Reedsville shale indicate that temperatures at this level exceeded at least 230 °C (Ar closure temperature for K-feldspar; Berger and York, 1981). This implies that the base of the folded cover stratigraphy in the Appalachians may have attained temperatures well above the central Andes but comparable to the Willard thrust in the Sevier belt (Fig. 16A). Finite strain measurements are limited for rocks below the cover stratigraphy detachment (one sample; Sak et al., 2012), but based on the thermal similarity to the Willard

thrust, we would predict large layer-normal flattening strains.

In the Appalachian Plateau, vitrinite reflectance from Pennsylvanian strata roughly indicate maximum temperatures of ~ 190 °C ($R_0 = 1.2$ – 1.4) at the Allegheny Front, diminishing to as low as 95 °C ($R_0 = 0.6$ – 1.0) at the western edge of the Appalachian Plateau (Barker, 1988; Ruppert et al., 2010). Lower deformation temperatures (100–160 °C) similar to the central Andes are estimated for the Devonian and Mississippian formations (Fig. 16B). The presence of a detectable tectonic strain in the Appalachian Plateau compared to the central Andes suggests that Appalachian Plateau deformation temperatures may have been slightly higher (closer to 160 °C), but as in the Sevier belt, differences in

Andean orocline strain and orogen-scale factors influencing grain-scale shortening

Figure 15. (A) Flinn diagram for Subandean (light gray) and Interandean (dark gray) finite ellipsoids. Ellipsoids with sub-horizontal Z axes are indicated by squares. White markers with crosses indicate ellipsoids with angular errors $>10^\circ$ in all three principal axes. Shaded area surrounding each point indicates the error region for k value defined by 100 Monte-Carlo ellipsoid simulations per sample based on two-dimensional (2-D) finite ellipse uncertainty. Ellipsoids with $k > 1$ are classified as prolate, exemplified by the theoretical ellipsoid above the vertical axis of the Flinn diagram. Samples with $k < 1$ are oblate, exemplified by the ellipsoid to the right of the horizontal axis. Octahedral shear strain contours are indicated by the dashed lines and are at intervals = 0.05. The k value contours are solid lines. (B) Flinn diagram for Eastern Cordillera finite ellipsoids. Symbology is the same as A.



mechanical stratigraphy may also explain the lack of central Andean strain at temperatures below $\sim 170\text{--}200^\circ\text{C}$.

Structurally, the Appalachian fold-and-thrust belt is similar to the Sevier belt because it only contains two major detachments in the Valley and Ridge (Ordovician Reedsville shale and Cambrian Waynesboro shale; Fig. 16B) and one

detachment in the Appalachian Plateau (Silurian Wills Creek and Salinas salt). As discussed in relation to the Sevier belt, the central Andes feature multiple detachment horizons but only two regionally extensive quartzite and sandstone formations thicker than 1 km (e.g., Ordovician San Benito and Devonian Vila Vila; Fig. 16B). These formations are classified as mechanically

strong (Fig. 3), but they lack the layer-parallel shortening strain fabric documented in Appalachian siliciclastic rocks (Sak et al., 2012) and predicted for shallow, strong rheologies (e.g., Sanderson, 1982; Yonkee, 2005). The stratigraphy accommodating layer-parallel shortening in the Appalachian Plateau consists of foreland basin siliciclastic sediments with interspersed

shale horizons that never exceed 500 m in thickness (Fig. 16A). Similar central Andean silicic lithologies at similar deformation temperatures lack layer-parallel shortening, as shown here. However, the Andean shale horizons feature weak penetrative strain features localized to the tip lines of thrust faults (McQuarrie and Davis, 2002). As suggested by comparing the Sevier and the central Andes, the thick central Andean marine shale units may have localized strain by forming regional detachments and limited strain accumulation in quartz-dominated lithologies (Fig. 16B). The Appalachian Plateau Silurian salt detachment also localizes strain, which is balanced by layer-parallel shortening and folding in the overlying siliciclastic rocks (Sak et al., 2012). However, the siliciclastic rocks remain unfaulted due to the inability of salt to fracture rock and form fault planes that cut up section (Jackson et al., 1994). In this case, the absence of thick shale horizons and resulting mechanical homogeneity of the Appalachian Plateau siliciclastic rocks may have favored strain accommodation by layer-parallel shortening rather than numerous, low-slip faults as seen in the central Andes.

In contrast to the Bolivian Andes, outcrop observations and thermochronology from northern Argentina document deformation temperatures >170 °C and pervasive pressure solution in siliciclastic lithologies (Pearson et al., 2012). Pearson et al. (2012) speculated that penetrative strain in mechanically strong basement rocks helped to accommodate shortening during Andean deformation in Argentina. Temperatures within the Cambrian metaturbidites and Ordovician granitoids were sufficient to reset AFT and partially reset ZHe Cenozoic cooling ages (Deeken et al., 2006; Pearson et al., 2012), indicating higher deformation temperatures than in the Bolivian Andes. While internal strain is not quantified for the Argentine Andes, temperatures up to ~ 180 °F during Andean deformation and the presence of dense cleavage are consistent with observations from thrust sheets in the Sevier belt, the Appalachian Valley and Ridge, and the Bhutanese Himalaya, where grain-scale shortening is on the order of 20%.

CONCLUSIONS

This study presents new 3-D finite strain data distributed across the width of the Andean fold-and-thrust belt and from various positions throughout the ~ 15 -km-thick stratigraphic section involved in deformation at the axis of the Bolivian orocline.

Our findings are:

(1) 3-D best-fit ellipsoids from across the region show uniformly low apparent strain mag-

nitudes ($\epsilon_s < 0.20$; 1.02:1:0.81). Average strain magnitudes range from $\epsilon_s = 0.03$ to 0.19 with uncertainties between 0.01 and 0.05. Ellipsoid shapes span the full range from prolate ($k \geq 1.0$) to oblate ($k < 1.0$), with k values from 0.1 to 22.3 that correspond to a range of triple-axial ratios ($X:Y:Z$) from 1.23:1:0.99 ($\epsilon_s = 0.17 \pm 0.01$, $k = 22.3 \pm 10$) to 1.02:1:0.81 ($\epsilon_s = 0.19 \pm 0.03$, $k = 0.1 \pm 0.1$).

(2) R_f - ϕ grain orientation data show angular variations in excess of 90° ($F = 108^\circ$ – 180°) and a wide range of axial ratios ($R_f = 1.0$ – 5.0). This indicates that the initial grain shapes overwhelm any measurable tectonic strain ($R_f > R_s$). Best-fit ellipse orientations for Fry data are very similar to R_f - ϕ data within uncertainty, and both are characterized by bedding-parallel long axes ($\phi < 30^\circ$). Ellipse axial ratios are also similar between methods, but best-fit R_f - ϕ ratios are usually higher by ~ 0.10 , most likely due to the wide variability in grain shape exhibited by most samples. Since the Fry method results are

less sensitive to grain variability at low strains, these results were used to calculate best-fit 3-D ellipsoids. Overall, the R_f - ϕ data show that most strain ellipse shapes are dominated by detrital grain geometry.

(3) Best-fit ellipsoids are dominantly oblate in shape, with Flinn's k value < 1 ($X = Y > Z$), placing them within the flattening strain field. The ellipsoid orientations are characterized by bedding-oblique to bedding-perpendicular Z axes and bedding-parallel Y and X axes. The oblate geometry, Z axes at high angles to bedding, and X axes within the bedding plane are equally consistent with either a detrital fabric related to sedimentation, or at most, a weak compaction strain during initial burial and lithification. At a minimum, the low strain magnitudes and ellipsoid shapes preclude significant bedding-parallel shortening at grain scale. As a result, any potential errors in bulk-shortening estimates for the central Andes are primarily a function of out-of-plane motion resulting from orocline

Figure 16 (on following two pages). (A) Comparative compilation of regional stratigraphy, strain, and temperature constraints from the central Andes and Sevier fold-and-thrust belt. The vertical axis is defined by an arbitrary geothermal gradient of 25 °C/km to appropriately scale the thickness of stratigraphic units. The stratigraphic columns are vertically positioned on the temperature scale based on the lowest temperature constraints available for the top of the stratigraphic column. Lines connect stratigraphic units to temperatures on the vertical axis at center based on deformation temperature constraints for that level. Shading of the temperature ranges is not specific, but light gray generally represents ~ 100 – 200 °C; middle gray is ~ 200 – 300 °C, and dark gray is for >300 °C. For the central Andes, alternating light and middle gray indicates that temperatures are not constrained to have exceeded ~ 180 °C. Arrows indicate whether a given temperature constraint is a minimum (deformation temperatures exceeded the constraint) or a maximum (deformation temperatures remained below the constraint). Temperature constraints in the Sevier belt are organized by thrust sheet since maximum deformation temperature varies by structural position in the fold-and-thrust belt. The west to east stacking order and the stratigraphy carried in each of the Sevier thrust sheets are shown at the right of the Sevier stratigraphy. For stratigraphic levels where strain data are available, the overall magnitude of strain is reported as the natural octahedral shear strain (ϵ_s) in the central Andes and bed-parallel strain (R_B) or mean strain (R_s) in the Sevier belt. For the Willard thrust, θ represents the angle between the principal stretch direction and bedding. The magnitude of out-of-plane strain is reported as the natural out-of-plane strain (ϵ_{OP}) for the central Andes and as layer-parallel shortening (LPS) for the Sevier belt. Black arrows indicate the stratigraphic position of detachment horizons. Central Andean lithologies are the same as Figure 3 (adapted from McQuarrie, 2002; McQuarrie and Davis, 2002). Sevier stratigraphy and structure was compiled from Coogan (1992), Yonkee et al. (1997), Yonkee (2005), DeCelles and Coogan (2006). Temperature constraints and references are listed in Table 4. (B) Comparative compilation of regional stratigraphy, strain, and temperature constraints from the central Andes and the Appalachians at the Pennsylvania salient. Central Andean stratigraphy, layout, and symbology are the same as A. Temperature constraints and references are listed in Table 4. For the Appalachians, the stratigraphic section, structural groupings (Appalachian Plateau, Valley and Ridge), and strain data are adapted from Sak et al. (2012). Appalachian finite strain is reported for each stratigraphic level as the mean strain (R_s) and the angle between the principal stretch direction (X axis) and bedding (θ). The regional layer-parallel shortening values for the structural regions are shown at right. Detachments for each region are indicated by black arrows.

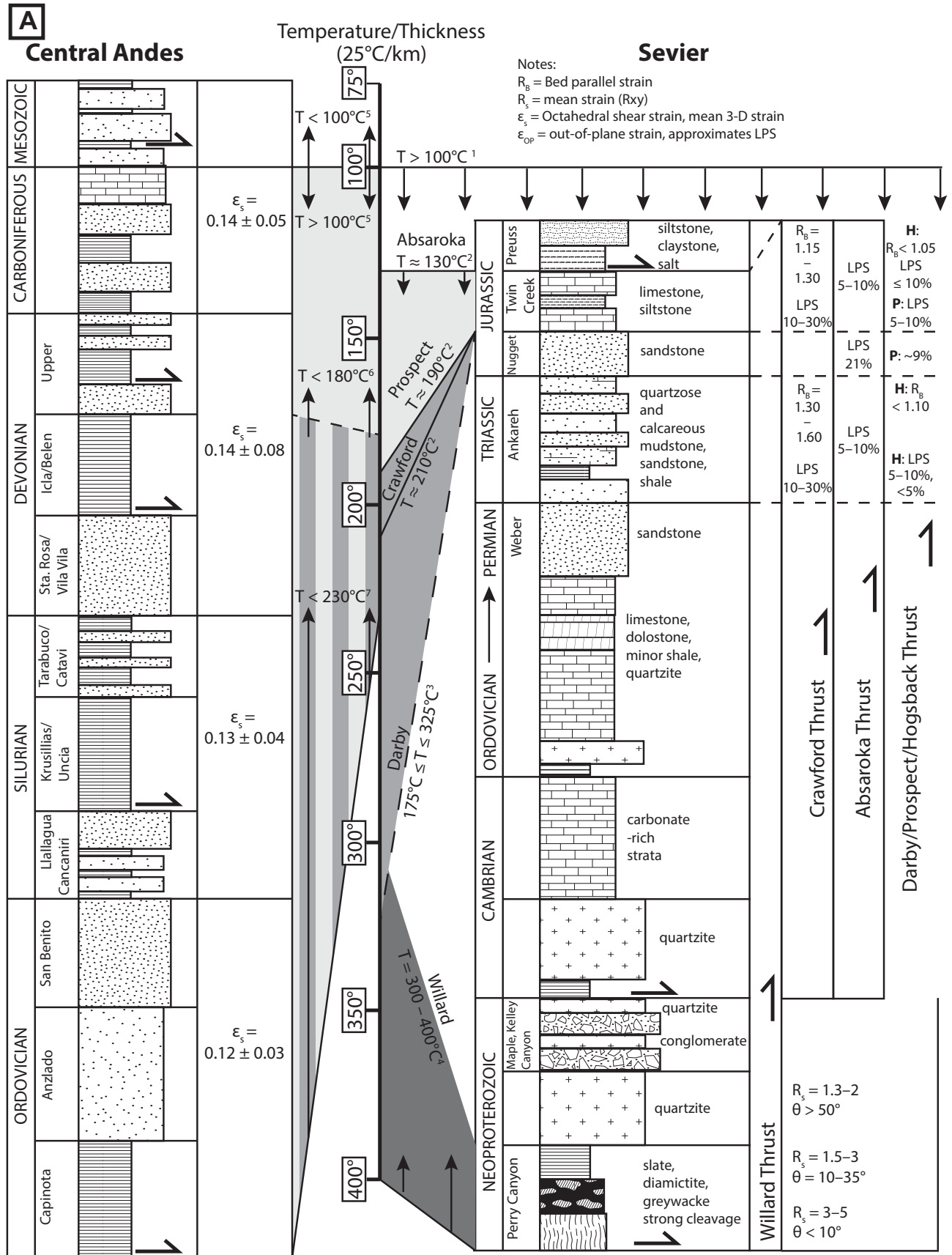


Figure 16.

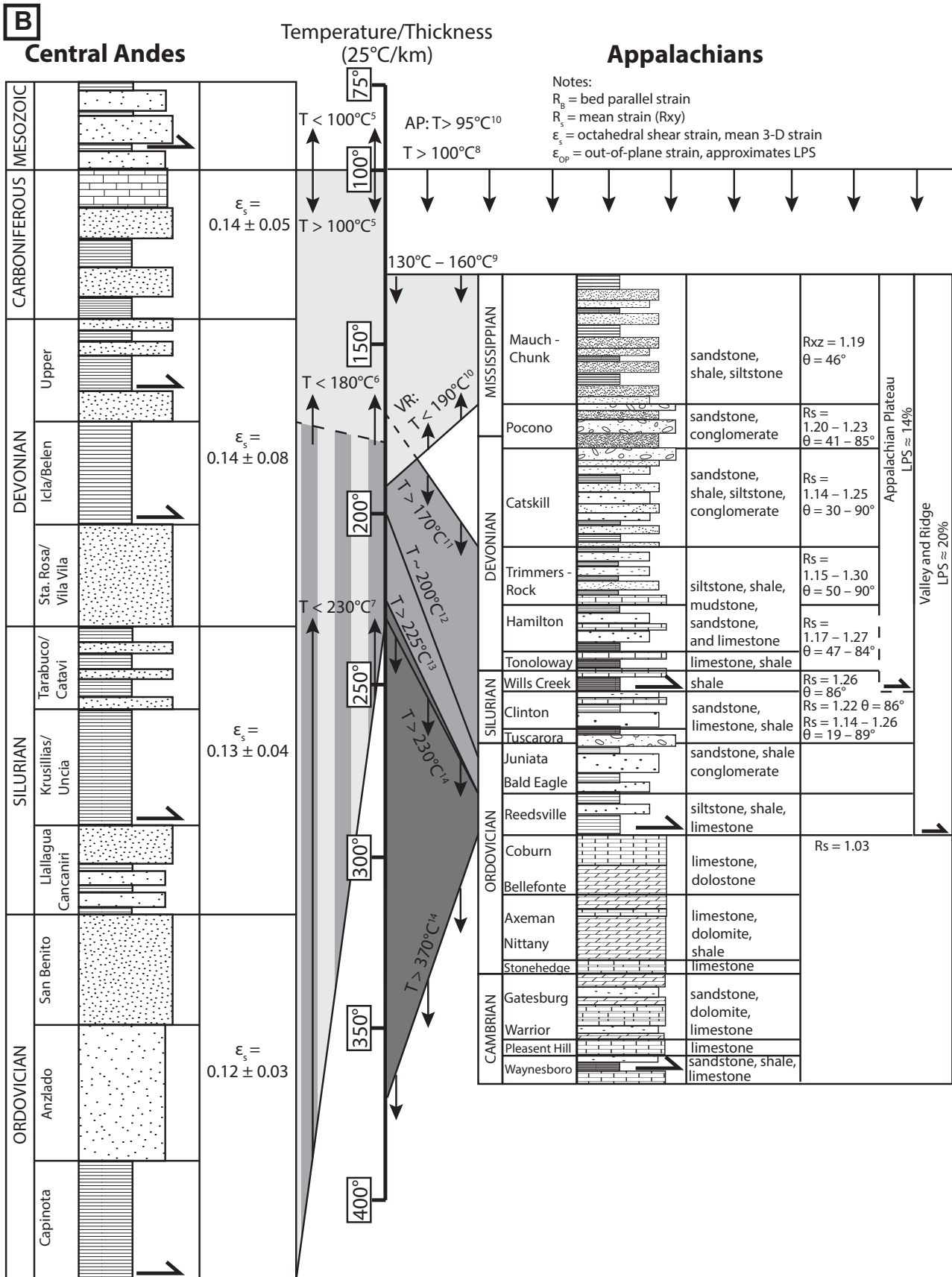


Figure 16 (continued).

Andean orocline strain and orogen-scale factors influencing grain-scale shortening

TABLE 4. SUMMARY OF STRATIGRAPHIC TEMPERATURE CONSTRAINTS

Number	Age	Stratigraphic unit	Structural position	Method	Temperature constraint (°C)	Reference
Central Andes						
1	Mesozoic		SA	Unreset AFT ages	<100	Barnes et al. (2008), Eichelberger et al. (2013)
2	Carboniferous Upper Devonian		SA SA	Unreset ZHe ages	<180	Eichelberger et al. (2013)
3	Devonian Silurian Ordovician	Vila Vila	IA EC IA, EC	Unreset ZFT ages	<230	Barnes et al. (2008)
Sevier						
4	Mesozoic– Precambrian		Prospect Darby Absaroka Meade Crawford Paris-Willard	Reset AFT ages	>100	Burtner and Nigrini (1994)
5	Jurassic	Twin Creek	Prospect Absaroka Crawford	Illite crystallinity	~190 ~130 ~210	Mitra and Yonkee (1985)
6	Jurassic	Twin Creek	Darby	Fluid inclusions	175–325	Wiltshcko et al. (2009)
7	Neoproterozoic		Willard	Reset Ar/Ar ages Fluid inclusions Illite crystallinity	300–500	Yonkee et al. (1989)
Appalachians						
8	Permian– Ordovician		AP VR	Reset AFT ages	>100	Blackmer et al. (1994)
9	Mississippian	Mauch Chunk	AP	Fluid inclusions Vitrinite reflectance	130–160	Reed et al. (2005)
10	Mississippian	Mauch Chunk	AP VR	Vitrinite reflectance Vitrinite reflectance	>95 <190	Ruppert et al. (2010) Ruppert et al. (2010)
11	Devonian	Trimmers Rock	VR	Fluid inclusions	>170	Evans (1995)
12	Ordovician	Bald Eagle	VR	Fluid inclusions	200	Lacazette (1991)
13	Ordovician	Trenton Formation	VR	Fluid inclusions	>225	Evans and Battles (1999)
14	Ordovician	Reedsville	Alleghany Front	Reset K-Ar age in Tuscarora fault mylonite*	>230 (T_c for K-feldspar) >370 (T_c for biotite)	Pierce and Armstrong (1966)

Note: Structural position abbreviations: SA—Subandes; IA—Interandean zone; EC—Eastern Cordillera; AP—Appalachians; VR—Valle and Ridge. Method abbreviations: AFT—apatite fission track; ZHe—(U-Th)/He; ZFT—zircon fission track.

*Reported mylonite mineralogy: 50% quartz, 38% illite, 10% carbonaceous material, 2% large-grain mica, abundant fine-grain mica (Pierce and Armstrong, 1966).

limb rotation and orogen-parallel displacements on transpressional or strike-slip faults.

(4) The preservation of detrital grain fabrics and/or compaction strains emphasizes the importance of deformation temperature in granular-scale processes that accommodate penetrative strain, such as dynamic recrystallization. The lack of quartz deformation textures and previously published thermochronology data indicate temperature conditions never exceeded ~240 °C and may have remained below 180 °C. These low temperatures would have limited the ability of the quartz-dominated lithologies to accommodate significant internal strains. Large layer-normal flattening strains are nonexistent in the central Andes but present in the Sevier thrust sheets of the western United States and Bhutanese Himalaya where deformation temperatures exceeded 230°. Layer-parallel shortening is best developed in regions of the Appalachians and Sevier belt where deformation temperatures reached or exceeded ~180 °C, the upper limit for central Andean deformation temperatures.

(5) The lack of appreciable layer-parallel shortening recorded in central Andean sandstones and quartzites relative to other fold-and-thrust belts appears to be related to differences in deformation temperature and mechanical stratigraphy. Strain, temperature, and stratigraphic data from the Sevier fold-and-thrust belt and the Appalachians suggest that deformation temperatures in the central Andes were insufficient to allow significant pressure solution, as indicated by low internal strain values and minimal cleavage development at the outcrop scale. The stratigraphy of the Bolivian orocline contains five regional detachments, including three ≥1-km-thick shale horizons. Comparatively, the Sevier and Appalachians only feature three major detachments and lack the thick continuous shale packages found in the central Andes. The dominance of mechanically weak stratigraphy in the Bolivian orocline may have localized strain along detachment horizons and resulted in the high density of low-offset thrust faults observed at the surface. Minimal fault

offset would have limited footwall burial and maintained low deformation temperatures, preventing significant internal strain accumulation.

ACKNOWLEDGMENTS

This research was supported in part by National Science Foundation (NSF) grant EAR-0908972 and Princeton University. Student field assistants from Bates College (Wes Farnsworth and Keegan Runnals), Princeton University (Andrew Budnick), and University of Pittsburgh (Lindsay Williams) were instrumental in sample collection and strain data development. SERGEOTECHMIN of La Paz, Bolivia, provided land access credentials and sampling permits. Jamie Tito and Sohrab Tawakoli aided in securing the required permits and made field work in Bolivia logistically possible. Matty Mookerjee provided valuable assistance with geologic programs for Mathematica. Additional thanks go to Frederick Vollmer for assistance with EllipseFit.

REFERENCES CITED

Allmendinger, R.W., Smalley, R., Bevis, M., Caprio, H., and Brooks, B., 2005, Bending the Bolivian orocline in real time: *Geology*, v. 33, p. 905–908, doi:10.1130/G21779.1.

- Allmendinger, R.W., Cardozo, N.C., and Fisher, D., 2013, Structural Geology Algorithms: Vectors & Tensors: Cambridge, UK, Cambridge University Press, 289 p.
- Armstrong, F.C., and Oriol, S.S., 1965, Tectonic development of Idaho-Wyoming thrust belt: American Association of Petroleum Geologists Bulletin, v. 49, p. 1847–1866.
- Arriagada, C., Roperch, P., Mpodozis, C., and Fernandez, R., 2006, Paleomagnetism and tectonics of the southern Atacama Desert (25–28°S), northern Chile: Tectonics, v. 25, TC4001, doi:10.1029/2005TC001923.
- Arriagada, C., Roperch, P., Mpodozis, C., and Cobbold, P.R., 2008, Paleogene building of the Bolivian orocline: Tectonic restoration of the central Andes in 2-D map view: Tectonics, v. 27, TC6014, doi:10.1029/2008TC002269.
- Baby, P., Moretti, L., Guillier, B., Limachi, R., Mendez, E., Oller, J., and Specht, M., 1995, Petroleum system of the northern and central Bolivian sub-Andean zone, in Tankard, A.J., Suárez S., R., and Welsink, H.J., Petroleum basins of South America: AAPG Memoir 62, p. 445–458.
- Barke, R., Lamb, S.H., and MacNiocaill, C., 2007, Late Cenozoic bending of the Bolivian Andes: New paleomagnetic and kinematic constraints: Journal of Geophysical Research, v. 112, B01101, doi:10.1029/2006JB004372.
- Barker, C.E., 1988, Geothermics of petroleum systems: Implications of the stabilization of kerogen thermal maturation after a geologically brief heating duration at peak temperature, in Magoon, L.B., ed., Petroleum Systems of the United States: U.S. Geological Survey Bulletin 1870, p. 26–29.
- Barnes, J.B., and Ehlers, T.A., 2009, End member models for Andean plateau uplift: Earth-Science Reviews, v. 97, p. 105–132, doi:10.1016/j.earscirev.2009.08.003.
- Barnes, J.B., Ehlers, T.A., McQuarrie, N., O'Sullivan, P.B., and Pelletier, J.D., 2006, Eocene to recent variations in erosion across the central Andean fold-thrust belt, northern Bolivia: Implications for plateau evolution: Earth and Planetary Science Letters, v. 248, p. 118–133, doi:10.1016/j.epsl.2006.05.018.
- Barnes, J.B., Ehlers, T.A., McQuarrie, N., O'Sullivan, P.B., and Tawackoli, S., 2008, Thermochronometer record of central Andean plateau growth, Bolivia (19.5°S): Tectonics, v. 27, TC3003, doi:10.1029/2007TC002174.
- Barnes, J.B., Ehlers, T.A., Insel, N., McQuarrie, N., and Poulsen, C.J., 2012, Linking orography, climate, and exhumation across the central Andes: Geology, 40, doi:10.1130/G33229.1.
- Benjamin, M.T., Johnson, N.M., and Naeser, C.W., 1987, Recent rapid uplift in the Bolivian Andes: Evidence from fission-track dating: Geology, v. 15, p. 680–683, doi:10.1130/0091-7613(1987)15<680:RRUITB>2.0.CO;2.
- Berger, G.W., and York, D., 1981, Geothermometry from ⁴⁰Ar/³⁹Ar dating experiments: Geochimica et Cosmochimica Acta, v. 45, p. 795–811, doi:10.1016/0016-7037(81)90109-5.
- Blackmer, G.C., Gornau, I.O., and Gold, D.P., 1994, Post-Alleghanian unroofing history of the Appalachian basin, Pennsylvania, from apatite fission track analysis and thermal models: Tectonics, v. 13, p. 1259–1276, doi:10.1029/94TC01507.
- Brandon, M.T., Roden-Tice, M.K., and Garver, J.I., 1998, Late Cenozoic exhumation of the Cascadia accretionary wedge in the Olympic Mountains, northwest Washington state: Geological Society of America Bulletin, v. 110, p. 985–1009, doi:10.1130/0016-7606(1998)110<0985:LCEOTC>2.3.CO;2.
- Burner, R.L., and Nigrini, A., 1994, Thermochronology of the Idaho-Wyoming thrust belt during the Sevier orogeny: A new, calibrated, multiprocess thermal model: American Association of Petroleum Geologists Bulletin, v. 78, p. 1586–1612.
- Cardozo, N., and Allmendinger, R.W., 2013, Spherical projections with OSXStereonet: Computers & Geosciences, v. 51, p. 193–205, doi:10.1016/j.cageo.2012.07.021.
- Carey, S.W., 1955, The orocline concept in geotectonics: Part I: Papers and Proceedings of the Royal Society of Tasmania, v. 89, p. 255–288.
- Coogan, J.C., 1992, Structural evolution of piggyback basins in the Wyoming-Idaho-Utah thrust belt, in Link, P.K., Kuntz, M.A., and Piatt, L.B., eds., Regional Geology of Eastern Idaho and Western Wyoming: Geological Society of America Memoir 179, p. 55–82, doi:10.1130/MEM179-p55.
- Craddock, J.P., 1992, Transpression during tectonic evolution of the Idaho-Wyoming fold-and-thrust belt, in Link, P.K., Kuntz, M.A., and Piatt, L.B., eds., Regional Geology of Eastern Idaho and Western Wyoming: Geological Society of America Memoir 179, p. 125–140, doi:10.1130/MEM179-p125.
- Crosby, G.W., 1969, Radial movements in the western Wyoming salient of the Cordilleran overthrust belt: Geological Society of America Bulletin, v. 80, p. 1061–1077, doi:10.1130/0016-7606(1969)80[1061:RMITWW]2.0.CO;2.
- DeCelles, P.G., and Coogan, J.C., 2006, Regional structure and kinematic history of the Sevier fold-and-thrust belt, central Utah: Geological Society of America Bulletin, v. 118, p. 841–864, doi:10.1130/B25759.1.
- Deeken, A., Sobel, E.R., Coutand, I., Haschke, M., Riller, U., and Strecker, M.R., 2006, Development of the southern Eastern Cordillera, NW Argentina, constrained by apatite fission track thermochronology: From Early Cretaceous extension to middle Miocene shortening: Tectonics, v. 25, TC6003, doi:10.1029/2005TC001894.
- Dewey, J.F., and Lamb, S.H., 1992, Active tectonics of the Andes: Tectonophysics, v. 205, p. 79–95.
- Dixon, J.S., 1982, Regional structural synthesis, Wyoming salient of western overthrust belt: American Association of Petroleum Geologists Bulletin, v. 66, p. 1560–1580.
- Duebendorfer, E.M., and Meyer, K.L., 2002, Penetrative strain at shallow crustal levels: The role of pressure solution in accommodating regional shortening strain, Ventura basin, western Transverse ranges, California, in Barth, A., ed., Contributions to Crustal Evolution of the Southwestern United States: Geological Society of America Special Paper 365, p. 295–314, doi:10.1130/0-8137-2365-5.295.
- Dunlap, W.J., Hirth, G., and Teyssier, C., 1997, Thermo-mechanical evolution of a ductile duplex: Tectonics, v. 16, p. 983–1000, doi:10.1029/97TC00614.
- Dunn, J.F., Hartshorn, K.G., and Hartshorn, P.W., 1995, Structural styles and hydrocarbon potential of the sub-Andean thrust belt of southern Bolivia, in Tankard, A.J., Suárez S., R., and Welsink, H.J., Petroleum Basins of South America: AAPG Memoir 62, p. 523–543.
- Dunne, W.M., Onasch, C.M., and Williams, R.T., 1990, The problem of strain-marker centers and the Fry method: Journal of Structural Geology, v. 12, p. 933–938, doi:10.1016/0191-8141(90)90067-9.
- Ege, H., Sobel, E.R., Scheuber, E., and Jacobshagen, V., 2007, Exhumation history of the southern Altiplano plateau (southern Bolivia) constrained by apatite fission-track thermochronology: Tectonics, v. 26, TC1004, doi:10.1029/2005TC001869.
- Eichelberger, N., McQuarrie, N., Ehlers, T.A., Enkelmann, E., Barnes, J.B., and Lease, R.O., 2013, New constraints on the chronology, magnitude, and distribution of deformation within the central Andean orocline: Tectonics, v. 32, p. 1432–1453, doi:10.1002/tect.20073.
- Elger, K., Oncken, O., and Glodny, J., 2005, Plateau-style accumulation of deformation: Southern Altiplano: Tectonics, v. 24, TC4020, doi:10.1029/2004TC001675.
- Engelder, T., 1979a, Mechanisms for strain within the Upper Devonian clastic sequence of the Appalachian Plateau, western New York: American Journal of Science, v. 279, p. 527–542, doi:10.2475/ajs.279.5.527.
- Engelder, T., 1979b, The nature of deformation within the outer limits of the central Appalachian foreland fold and thrust belt in New York State: Tectonophysics, v. 55, p. 289–310, doi:10.1016/0040-1951(79)90181-1.
- Erslev, E.A., 1988, Normalized center-to-center strain analysis of packed aggregates: Journal of Structural Geology, v. 10, p. 201–209, doi:10.1016/0191-8141(88)90117-4.
- Evans, M.A., 1995, Fluid inclusions in veins from the middle Devonian shales: A record of deformation conditions and fluid evolution in the Appalachian Plateau: Geological Society of America Bulletin, v. 107, p. 327–339, doi:10.1130/0016-7606(1995)107<0327:FIIVFT>2.3.CO;2.
- Evans, M.A., and Battles, D.A., 1999, Fluid inclusion and stable isotope analyses of veins from the central Appalachian Valley and Ridge Province: Implications for regional synorogenic hydrologic structure and fluid migration: Geological Society of America Bulletin, v. 111, p. 1841–1860, doi:10.1130/0016-7606(1999)111<1841:FIASIA>2.3.CO;2.
- Fail, R.T., and Nickelsen, R.P., 1999, Appalachian mountain section of the Valley and Ridge Province, in Schultz, C.H., ed., The Geology of Pennsylvania: Geological Survey of Pennsylvania Special Publication 1, p. 268–285.
- Fisher, N.I., Lewis, T.L., and Embleton, B.J., 1987, Statistical Analysis of Spherical Data: Cambridge, UK, Cambridge University Press, 329 p.
- Fitzgibbon, A., Pilu, M., and Fisher, R.B., 1999, Direct least square fitting of ellipses: IEEE Pattern Analysis and Machine Intelligence, v. 21, p. 476–480, doi:10.1109/34.765658.
- Flinn, D., 1962, On folding during three-dimension progressive deformation: Quarterly Journal of the Geological Society of London, v. 118, p. 385–428, doi:10.1144/gsjgs.118.1.0385.
- Fry, N., 1979, Density distribution techniques and strained length methods for determination of finite strains: Journal of Structural Geology, v. 1, p. 221–229, doi:10.1016/0191-8141(79)90041-5.
- Gal, O., 2003, Fit_ellipse: <http://www.mathworks.com/matlabcentral/fileexchange/3215-fitellipse>, MATLAB Central File Exchange (accessed 14 August 2011).
- Geiser, P.A., and Engelder, T., 1983, The distribution of layer parallel shortening fabrics in the Appalachian foreland of New York and Pennsylvania: Evidence for two non-coaxial phases of the Alleghanian orogeny, in Hatcher, R.D., Jr., Williams, H., and Zietz, I., eds., Contributions to the Tectonics and Geophysics of Mountain Chains: Geological Society of America Memoir 158, p. 161–175.
- Gillis, R.J., Horton, B.K., and Grove, M., 2006, Thermochronology, geochronology, and upper crust structure of the Cordillera Real: Implications for Cenozoic exhumation of the central Andean plateau: Tectonics, v. 25, TC6007, doi:10.1029/2005TC001887.
- Gockley, C.K., 1985, Structure and Strain Analysis of the Big Elk Mountain Anticline, Caribou Mountains, Idaho [M.S. thesis]: Boulder, Colorado, University of Colorado, 221 p.
- González, M., Díaz-Martínez, E., and Tiella, L., 1996, Comentarios sobre la estratigrafía del Silúrico y Devónico del norte y centro de la Cordillera Oriental y Altiplano de Bolivia: Simposio Sul Americano do Siluro-Devoniano, Ponta Grossa, Brazil, p. 117–130.
- Gray, M.B., and Mitra, G., 1993, Migration of deformation fronts during progressive deformation: evidence from detailed structural studies in the Pennsylvania anthracite region, U.S.A.: Journal of Structural Geology, v. 15, p. 435–449, doi:10.1016/0191-8141(93)90139-2.
- Hindle, D., Kley, J., Oncken, O., and Sobolev, S., 2005, Crustal balance and crustal flux from shortening estimates in the central Andes: Earth and Planetary Science Letters, v. 230, p. 113–124, doi:10.1016/j.epsl.2004.11.004.
- Hirth, G., and Tullis, J., 1992, Dislocation creep regimes in quartz aggregates: Journal of Structural Geology, v. 14, no. 2, p. 145–159, doi:10.1016/0191-8141(92)90053-Y.
- Hirth, G., and Tullis, J., 1994, The brittle-plastic transition in experimentally deformed quartz aggregates: Journal of Geophysical Research, v. 99, p. 11,731–11,748, doi:10.1029/93JB02873.
- Houseknecht, D.W., 1988, Intergranular pressure solution in four quartzose sandstones: Journal of Sedimentary Petrology, v. 58, p. 228–246.
- Imlay, R.W., 1967, Twin Creek Limestone (Jurassic) in the Western Interior of the United States: U.S. Geological Survey Professional Paper 540, 105 p.
- Isacks, B.L., 1988, Uplift of the central Andean Plateau and bending of the Bolivian orocline: Journal of Geophysical Research, v. 93, p. 3211–3231, doi:10.1029/JB093iB04p03211.
- Jackson, M.P.A., Vendeville, B.C., and Schultz-Ela, D.D., 1994, Structural dynamics of salt systems: Annual Review of Earth and Planetary Sciences, v. 22, p. 93–117, doi:10.1146/annurev.earth.22.050194.000521.
- Jaeger, J.C., and Cook, N.G.W., 1979, Fundamentals of Rock Mechanics, 3rd ed., Chapman and Hall, London, U.K.

Andean orocline strain and orogen-scale factors influencing grain-scale shortening

- Kamb, W.B., 1959, Ice petrofabric observations from Blue Glacier, Washington, in relation to theory and experiment: *Journal of Geophysical Research*, v. 64, p. 1891–1909, doi:10.1029/JZ064i01p01891.
- Kley, J., 1996, Transition from basement-involved to thin-skinned thrusting in the Cordillera Oriental of southern Bolivia: *Tectonics*, v. 15, p. 763–775, doi:10.1029/95TC03868.
- Kley, J., 1999, Geologic and geometric constraints on a kinematic model of the Bolivian orocline: *Journal of South American Earth Sciences*, v. 12, p. 221–235, doi:10.1016/S0895-9811(99)00015-2.
- Kley, J., and Monaldi, C.R., 1998, Tectonic shortening and crustal thickness in the central Andes; how good is the correlation?: *Geology*, v. 26, p. 723–726, doi:10.1130/0091-7613(1998)026<0723:TSACTI>2.3.CO;2.
- Kummel, B., 1954, Triassic Stratigraphy of Southeastern Idaho and Adjacent Areas: U.S. Geological Survey Professional Paper 0254-H, p. 165–194.
- Lacazette, A.J., Jr., 1991, Natural Hydraulic Fracturing in the Bald Eagle Sandstone in Central Pennsylvania and the Ithaca Siltstone at Watkins Glen, New York [Ph.D. thesis]: University Park, Pennsylvania, Pennsylvania State University, 225 p.
- Long, S., McQuarrie, N., Tobgay, T., and Hawthorne, J., 2011, Quantifying internal strain and deformation temperature in the eastern Himalaya, Bhutan; implications for the evolution of strain in thrust sheets: *Journal of Structural Geology*, v. 33, p. 579–608, doi:10.1016/j.jsg.2010.12.011.
- Long, S., McQuarrie, N., Tobgay, T., Coutand, I., Cooper, F.J., Reiners, P.W., Wartho, J.A., and Hodges, K.V., 2012, Variable shortening rates in the eastern Himalayan thrust belt, Bhutan; insights from multiple thermochronologic and geochronologic data sets tied to kinematic reconstructions: *Tectonics*, v. 31, TC5004, doi:10.1029/2012TC003155.
- Marshak, S., 1988, Kinematics of orocline and arc formation in thin-skinned orogens: *Tectonics*, v. 7, no. 1, p. 73–86.
- McNaught, M.A., and Mitra, G., 1996, The use of finite strain data in constructing a retrodeformable cross-section of the Meade thrust sheet, southeastern Idaho, U.S.A.: *Journal of Structural Geology*, v. 18, p. 573–583, doi:10.1016/S0191-8141(96)80025-3.
- McQuarrie, N., 2002, The kinematic history of the central Andean fold-thrust belt, Bolivia; implications for building a high plateau: *Geological Society of America Bulletin*, v. 114, p. 950–963, doi:10.1130/0016-7606(2002)114<0950:TKHOTC>2.0.CO;2.
- McQuarrie, N., and Davis, G.H., 2002, Crossing the several scales of strain-accomplishing mechanisms in the hinterland of the central Andean fold-thrust belt, Bolivia: *Journal of Structural Geology*, v. 24, p. 1587–1602, doi:10.1016/S0191-8141(01)00158-4.
- McQuarrie, N., and DeCelles, P., 2001, Geometry and structural evolution of the central Andean backthrust belt, Bolivia: *Tectonics*, v. 20, p. 669–692, doi:10.1029/2000TC001232.
- McQuarrie, N., Barnes, J.B., and Ehlers, T.A., 2008, Geometric, kinematic, and erosional history of the central Andean plateau, Bolivia (15–17°S): *Tectonics*, v. 27, TC3007, doi:10.1029/2006TC002054.
- Means, W.D., 1989, Stretching faults: *Geology*, v. 17, p. 893–896, doi:10.1130/0091-7613(1989)017<0893:SF>2.3.CO;2.
- Mitra, G., 1994, Strain variation in thrust sheets across the Sevier fold-and-thrust belt (Idaho-Utah-Wyoming); implications for section restoration and wedge taper evolution: *Journal of Structural Geology*, v. 16, p. 585–602, doi:10.1016/0191-8141(94)90099-X.
- Mitra, G., and Yonkee, W.A., 1985, Relationship of spaced cleavage to folds and thrusts in the Idaho-Utah-Wyoming thrust belt: *Journal of Structural Geology*, v. 7, p. 361–373, doi:10.1016/0191-8141(85)90041-0.
- Moore, M., and Nickleach, S., 2011, Three-dimensional strain analysis using Mathematica: *Journal of Structural Geology*, v. 33, p. 1467–1476, doi:10.1016/j.jsg.2011.08.003.
- Moretti, I., Baby, P., Mendez, E., and Zubieta, D., 1996, Hydrocarbon generation in relation to thrusting in the Sub Andean zone from 18° to 22°S, Bolivia: *Petroleum Geoscience*, v. 2, p. 17–28.
- Mukul, M., and Mitra, G., 1998, Finite strain and strain variation analysis in the Sheeprock thrust sheet; an internal thrust sheet in the Provo salient of the Sevier fold-and-thrust belt, central Utah: *Journal of Structural Geology*, v. 20, no. 4, p. 385–405, doi:10.1016/S0191-8141(97)00087-4.
- Müller, J.P., Kley, J., and Jacobshagen, V., 2002, Structure and Cenozoic kinematics of the Eastern Cordillera, southern Bolivia (21°S): *Tectonics*, v. 21, 1037, doi:10.1029/2001TC001340.
- Nadai, A., 1963, Theory of Flow and Fracture of Solids: Engineering Societies Monographs: New York, McGraw-Hill, 705 p.
- Nickelsen, R.P., 1963, Fold patterns and continuous deformation mechanisms of the central Pennsylvania folded Appalachians, in Cate, A.S., ed., *Tectonics and Cambrian-Ordovician Stratigraphy in the Central Appalachians of Pennsylvania*: Pittsburgh, Pennsylvania, Pittsburgh Geological Society, Guidebook, p. 13–29.
- Nickelsen, R.P., 1983, Aspects of Alleghanian deformation, in Nickelsen, R.P., and Cotter, E., eds., *Silurian Depositional History and Alleghanian Deformation in the Pennsylvania Valley and Ridge*: 49th Field Conference of Pennsylvania Geologists: Danville, Pennsylvania, Guidebook, Pennsylvania Geological Society, p. 29–39.
- Ong, P.F., van der Pluijm, B.A., and Van der Voo, R., 2007, Early rotation and late folding in the Pennsylvania salient (U.S. Appalachians); evidence from calcite-twinning analysis of Paleozoic carbonates: *Geological Society of America Bulletin*, v. 119, p. 796–804, doi:10.1130/B26013.1.
- Pearson, D.M., Kapp, P., Reiners, P.W., Gehrels, G.E., Ducea, M.N., Pullen, A., Otamendi, J.E., and Alonso, R.N., 2012, Major Miocene exhumation by fault-propagation folding within a metamorphosed, early Paleozoic thrust belt; northwestern Argentina: *Tectonics*, v. 31, TC4023, doi:10.1029/2011TC003043.
- Pfiffner, O.A., and Ramsay, J.G., 1982, Constraints on geological strain rates: arguments from finite strain states of naturally deformed rocks: *Journal of Geophysical Research*, v. 87, p. 311–321, doi:10.1029/JB087iB01p00311.
- Pierce, K.L., and Armstrong, R.L., 1966, Tuscarora fault; an Acadian(?) bedding-plane fault in central Appalachian Valley and Ridge Province: *American Association of Petroleum Geologists Bulletin*, v. 50, p. 385–390.
- Poirier, J.P., Guillope, M., Nicolas, A., Darot, M., and Wil-laime, C., 1979, Deformation induced recrystallization of minerals: *Bulletin de Mineralogie*, v. 102, p. 67–74.
- Ramsay, J.G., 2000, A strained Earth, past and present: *Science*, v. 288, p. 2139–2141, doi:10.1126/science.288.5474.2139.
- Ramsay, J.G., and Huber, M.I., 1983, *Techniques of Modern Structural Geology: Strain Analysis, Volume 1*: London, Academic Press, 307 p.
- Reed, J.S., Spotila, J.A., Eriksson, K.A., and Bodnar, R.J., 2005, Burial and exhumation history of Pennsylvanian strata, central Appalachian basin; an integrated study: *Basin Research*, v. 17, p. 259–268, doi:10.1111/j.1365-2117.2005.00265.x.
- Reiners, P.W., Spell, T.L., Nicolescu, A., and Zanetti, K.A., 2004, Zircon (U-Th)/He thermochronometry: He diffusion and comparisons with ⁴⁰Ar/³⁹Ar dating: *Geochimica et Cosmochimica Acta*, v. 68, p. 1857–1887, doi:10.1016/j.gca.2003.10.021.
- Ries, A.C., and Shackleton, R.M., 1976, Patterns of strain variation in arcuate fold belts: *Philosophical Transactions of the Royal Society of London, ser. A, Mathematical and Physical Sciences*, v. 283, p. 281–288, doi:10.1098/rsta.1976.0085.
- Roden, M.K., 1991, Apatite fission-track thermochronology of the southern Appalachian basin; Maryland, West Virginia, and Virginia: *The Journal of Geology*, v. 99, p. 41–53, doi:10.1086/629472.
- Roden, M.K., Miller, D.S., Gardner, T.W., and Sevon, W.D., 1989, Apatite fission-track thermochronology of the Pennsylvania Appalachian basin: *Geomorphology*, v. 2, p. 39–51, doi:10.1016/0169-555X(89)90005-6.
- Roeder, D., and Chamberlain, R.L., 1995, Structural geology of sub-Andean fold and thrust belt in northwestern Bolivia, in Tankard, A.J., Suarez, R., and Welsink, H.J., eds., *Petroleum Basins of South America: Ameri-*
- can Association of Petroleum Geologists Memoir 62, p. 459–479.
- Roperch, P., Sempere, T., Macedo, A., Arriagada, C., Fornari, M., Tapia, C., Garcia, M., and Laj, C., 2006, Counterclockwise rotation of late Eocene-Oligocene fore-arc deposits in southern Peru and its significance for oroclinal bending in the central Andes: *Tectonics*, v. 25, TC3010, doi:10.1029/2005TC001882.
- Royle, F., 1993, An overview of the geologic structure of the thrust belt in Wyoming, northern Utah, and eastern Idaho, in Snoke, A.W., Stiedtmann, J.R., and Roberts, S.M., eds., *Geology of Wyoming: Geological Survey of Wyoming Memoir 5*, p. 272–311.
- Royle, F., Warner, M.A., and Reese, D.L., 1975, Thrust belt structural geometry and related stratigraphic problems, Wyoming-Idaho-northern Utah, in Boylard, E.W., ed., *Deep Drilling Frontiers of the Central Rocky Mountains*: Denver, Rocky Mountain Association of Geologists, p. 41–45.
- Ruppert, L.F., Hower, J.C., Ryder, R.T., Levine, J.R., Trippi, M.H., and Grady, W.C., 2010, Geologic controls on thermal maturity patterns in Pennsylvanian coal-bearing rocks in the Appalachian basin: *International Journal of Coal Geology*, v. 81, p. 169–181, doi:10.1016/j.coal.2009.12.008.
- Rutter, E.H., 1976, The kinetics of rock deformation by pressure solution: *Philosophical Transactions of the Royal Society of London, ser. A, Mathematical and Physical Sciences*, v. 283, p. 203–219, doi:10.1098/rsta.1976.0079.
- Sak, P.B., McQuarrie, N., Oliver, B.P., Lavdovsky, N., and Jackson, M.S., 2012, Unraveling the central Appalachian fold-thrust belt, Pennsylvania; The power of sequentially restored balanced cross sections for a blind fold-thrust belt: *Geosphere*, v. 8, p. 685–702, doi:10.1130/GES00676.1.
- Sanderson, D.J., 1982, Models of strain variation in nappes and thrust sheets; a review: *Tectonophysics*, v. 88, p. 201–233, doi:10.1016/0040-1951(82)90237-2.
- Schmid, S.M., and Handy, M.R., 1991, Towards a genetic classification of fault rocks; geological usage and tectonophysical implications, in Müller, D.W., McKenzie, J.A., and Weissert, H., eds., *Controversies in Modern Geology*: London, Academic Press, p. 339–361.
- Sempere, T., 1994, Kimmeridgian? to Paleocene tectonic evolution of Bolivia, in Salfity, J.A., ed., *Cretaceous Tectonics of the Andes*: Wiesbaden, Germany, Vieweg Publishing, p. 168–212, doi:10.1007/978-3-322-85472-8_4.
- Sempere, T., 1995, Phanerozoic evolution of Bolivia and adjacent regions, in Tankard, A.J., Suarez, R., and Welsink, H.J., eds., *Petroleum Basins of South America: American Association of Petroleum Geologists Memoir 62*, p. 207–230.
- Sheffels, B.M., 1988, Structural Constraints on Structural Shortening in the Bolivian Andes [Ph.D. thesis]: Cambridge, Massachusetts, Massachusetts Institute of Technology, 167 p.
- Shimamoto, T., and Ikeda, Y., 1976, A simple algebraic method for strain estimation for deformed ellipsoidal objects: 1. Basic theory: *Tectonophysics*, v. 36, p. 315–337, doi:10.1016/0040-1951(76)90107-4.
- Slaughter, J.A., 1982, Fossil Distortion and Pressure Solution in the Middle to Upper Devonian Clastics and Limestones of the Appalachian Plateau, Central New York [M.S. thesis]: Storrs, Connecticut, University of Connecticut, 32 p.
- Somoza, R., Singer, S., and Coira, B., 1996, Paleomagnetism of Upper Miocene ignimbrites at the Puna; an analysis of vertical-axis rotations in the central Andes: *Journal of Geophysical Research*, v. 101, p. 11,387–11,400, doi:10.1029/95JB03467.
- Stipp, M., Stuenzli, H., Heilbronner, R., and Schmid, S.M., 2002, The eastern Tonalé fault zone: a “natural laboratory” for crystal plastic deformation of quartz over a temperature range from 250 to 700 °C: *Journal of Structural Geology*, v. 24, p. 1861–1884, doi:10.1016/S0191-8141(02)00035-4.
- Stöckhert, B., Brix, M.R., Kleinschrodt, R., Hurford, A.J., and Wirth, R., 1999, Thermochronometry and microstructures of quartz; a comparison with experimental flow laws and predictions on the temperature of the

- brittle-plastic transition: *Journal of Structural Geology*, v. 21, p. 351–369, doi:10.1016/S0191-8141(98)00114-X.
- van Daalen, M., Heilbronner, R., and Kunze, K., 1999, Orientation analysis of localized shear deformation in quartz fibres at the brittle-ductile transition: *Tectonophysics*, v. 303, p. 83–107, doi:10.1016/S0040-1951(98)00264-9.
- van der Pluijm, B.A., and Marshak, S., 2004, *Earth Structure: An Introduction to Structural Geology and Tectonics*: New York, W.W. Norton & Company, 672 p.
- Voll, G., 1976, Recrystallization of quartz, biotite and feldspars from Erstfeld to the Leventina nappe, Swiss Alps, and its geological significance: *Schweizerische Mineralogische und Petrographische Mitteilungen*, v. 56, p. 641–647.
- Vollmer, F.W., 2010, A comparison of ellipse-fitting techniques for two and three-dimensional strain analysis, and their implementation in an integrated computer program designed for field-based studies: Abstract T21B-2166, Fall Meeting, American Geophysical Union, San Francisco, California.
- Vollmer, F.W., 2011a, EllipseFit 2.0: <http://www.frederickvollmer.com/ellipsefit/> (accessed 9 January 2014).
- Vollmer, F.W., 2011b, Best-fit strain from multiple angles of shear and implementation in a computer program for geological strain analysis: *Geological Society of America Abstracts with Programs*, v. 43, no. 1, p. 147.
- Watts, A.B., Lamb, S.H., Fairhead, J.D., and Dewey, J.F., 1995, Lithospheric flexure and bending of the Central Andes: *Earth Planetary Science Letters*, v. 134, p. 9–21.
- Weil, A.B., and Sussman, A.J., 2004, Classifying curved orogens based on timing relationships between structural development and vertical-axis rotations, *in* Sussman, A.J., and Weil, A.B., eds., *Orogenic Curvature: Integrating Paleomagnetic and Structural Analyses*: Geological Society of America Special Paper 383, p. 1–17.
- Weil, A.B., and Yonkee, W.A., 2012, Layer-parallel shortening across the Sevier fold-thrust belt and Laramide foreland of Wyoming; spatial and temporal evolution of a complex geodynamic system: *Earth and Planetary Science Letters*, v. 357–358, p. 405–420, doi:10.1016/j.epsl.2012.09.021.
- Weil, A.B., Yonkee, W.A., and Sussman, A., 2010, Reconstructing the kinematic evolution of curved mountain belts: A paleomagnetic study of Triassic red beds from the Wyoming salient, Sevier thrust belt, U.S.A.: *Geological Society of America Bulletin*, v. 122, no. 1–2, p. 3–23, doi:10.1130/B26483.1.
- Welsink, H.J., Franco, M.A., and Oviedo, G.C., 1995, Andean and pre-Andean deformation, Boomerang Hills area, Bolivia, *in* Tankard, A.J., Suarez, R., and Welsink, H.J., eds., *Petroleum Basins of South America*: American Association of Petroleum Geologists Memoir 62, p. 481–499.
- Wiltschko, D.V., Lambert, G.R., and Lamb, W., 2009, Conditions during syntectonic vein formation in the footwall of the Absaroka thrust fault, Idaho-Wyoming-Utah fold and thrust belt: *Journal of Structural Geology*, v. 31, p. 1039–1057, doi:10.1016/j.jsg.2009.03.009.
- Yonkee, W.A., 2005, Strain patterns within part of the Willard thrust sheet, Idaho-Utah-Wyoming thrust belt: *Journal of Structural Geology*, v. 27, p. 1315–1343, doi:10.1016/j.jsg.2004.06.014.
- Yonkee, W.A., and Weil, A.B., 2010, Reconstructing the kinematic evolution of curved mountain belts; internal strain patterns in the Wyoming salient, Sevier thrust belt, U.S.A.: *Geological Society of America Bulletin*, v. 122, p. 24–49, doi:10.1130/B26484.1.
- Yonkee, W.A., Parry, W.T., Bruhn, R.L., 1989, Thermal models of thrust faulting: Constraints from fluid-inclusion observations, Willard thrust sheet, Idaho-Utah-Wyoming thrust belt: *Geological Society of America Bulletin*, v. 101, no. 2, p. 304–313, doi:10.1130/0016-7606(1989)101<0304:TMOTFC>2.3.CO;2.
- Yonkee, W.A., DeCelles, P.G., and Coogan, J., 1997, Kinematics and synorogenic sedimentation of the eastern frontal part of the Sevier orogenic wedge, northern Utah, *in* Link, P.K., and Kowallis, B.K., eds., *Proterozoic to Recent Stratigraphy, Tectonics, and Volcanology, Utah, Nevada, Southern Idaho, and Central Mexico*: Brigham Young University Studies, v. 42, p. 355–380.

SCIENCE EDITOR: CHRISTIAN KOEBERL
ASSOCIATE EDITOR: STEFANO MAZZOLI

MANUSCRIPT RECEIVED 17 JULY 2013
REVISED MANUSCRIPT RECEIVED 14 MAY 2014
MANUSCRIPT ACCEPTED 16 JUNE 2014

Printed in the USA